Elucidating Solvent Effects on the Solution Processing of Methyl Ammonium Lead Iodide Perovskites Using Molecular Modelling Approaches

A Thesis

Presented to the Faculty of the Graduate School

of Cornell University

in Partial Fulfillment of the Requirements for the Degree of

Master of Science

by

Oluwaseun Victor Romiluyi

August 2019

ABSTRACT

When processed in solution, Hybrid Organic–Inorganic Perovskite (HOIP)–based solar cells, provide a unique cost advantage over existing solar cell technologies. However, the morphology of the final crystal film is known to be heavily influenced by solvent selection – and these effects remain poorly understood. Studying the nucleation and early stage growth of these materials in solution would provide much needed insight into the effect of solvents on final film morphology. Molecular simulation models and techniques have a significant role to play in this endeavour by uncovering the solvent–solute interactions influencing the formation of moieties that will ultimately nucleate and grow into thin films. My project involves the generation of models that are capable of accurately predicting the efficacy of certain solvents in the solution processing of lead iodide perovskites. The goal of this project is to utilize these models to develop a comprehensive understanding of solvent influence on thin film growth.

BIOGRAPHICAL SKETCH

Oluwaseun (Seun) Victor Romiluyi was born in Lagos, Nigeria in 1996. He lived in Nigeria up to the age of 5, before relocating to Humble, Texas in the United States. After 5 years in Texas, Seun returned to Nigeria with his family. Spending his childhood years in these to locations allowed Seun to learn from two distinctive educational systems – which sharpened his reasoning skills and expanded his creativity. After spending another 6 years in Nigeria, he completed his secondary education at Greenspring School Lagos – and over that time he developed a passion for science and mathematics. He then moved to Hamilton, Ontario in Canada, where finished another year of high school at Columbia International College (CIC), and began his undergraduate studies at McMaster University in the same year, 2013. Seun graduated from McMaster University with his Bachelor of Engineering in Chemical Engineering in 2017 before moving to Ithaca, NY in August of that year to pursue his graduate studies at the School of Chemical and Biomolecular Engineering of Cornell University.

In June 2018, he was awarded the GEM University Fellowship by the GEM consortium due to his academic and community achievements at Cornell. He was also nominated for first year student of year at the Diversity Programs in Engineering (DPE) annual banquet. Outside research, Seun is involved in Diversity and Inclusion Program (DIP), a new initiative in the Smith School focused on improving the climate and building the community in Olin Hall. He was a summer camp instructor for the DPEs CATALYST program for high school students interested in STEM fields, and he continues to remain engaged in efforts aiming to improve the culture of his community.

Upon the completion of his M.S. degree, Seun will continue as a Ph.D. student under the tutelage of Prof. Paulette Clancy.

This thesis is dedicated to my family and friends.

ACKNOWLDEGEMENTS

I would like to thank my advisor, Prof. Paulette Clancy for all the support that she has provided during this program. Her guidance and open mindedness are exemplary of any professional that I have come across, and I am very grateful to have such an amazing mentor. I would also like to thank Clay Hamil and Dr. Lynn Loo, our experimental collaborators at Princeton University. Prof. Tobias Harnath, my committee member, for his support towards the completion of this thesis, and give a special thanks to the Institute of Computational Science and Engineering at Cornell for providing me with the computational resources to conduct these experiments. I would personally like to thank Prof. Li Xi at McMaster University for introducing me to computational chemistry as an undergraduate student in his lab and for his continued support throughout my graduate studies. Stéphie–Anne C. Dulièpre for her unending support, care, encouragement and inspiration throughout my journey here. And finally, I would like to thank my loving family for being the motivation to my pursuit of knowledge. Oyinkan, for always being there for support and advise throughout this academic journey. And Mom and Dad, you guys continue to push me and inspire me to be the best I can be, I will always be grateful for that.

TABLE OF CONTENTS

LIST OF TABLES

LIST OF FIGURES

CHAPTER 1

INTRODUCTION

1.1 Overview of Photovoltaic Solar Cells

With the looming threat of climate change, there is a tremendous impetus to find solutions that facilitate the transition from fossil fuels to 'greener' initiatives. Solar power (along with wind, nuclear, and geothermal technology) has been considered as one of these green alternatives. And due to solar irradiance, 1000 W/m^2 of power from the sun impacts the earth's surface [1], offering a huge potential of energy that could potentially be extracted from this source. Solar technology has emerged to capture the energy from the sun – in the form of both solar thermal and photovoltaic (PV) energy – to generate electricity [1]. Solar thermal energy technology like solar updraft towers [2–4], space heating and cooling [5, 6] are examples of devices that leverage the sun's thermal power, while PV devices are technologies that utilize light particles from the sun, called photons, to generate electricity. Only semiconductor materials that exhibit the photovoltaic effect are well suited for this application [7].

The introduction of commercial PV devices coincided with the growth and development of silicon electronics in the 1950s [8]. The first silicon solar cell was reported in 1954 with a mere 6% efficiency [9]. The high cost of fabrication and low Solar Conversion Efficiency (SCE) made these devices of interest, but only to space applications such as satellites where the cost was relatively unimportant [10]. In the years that followed, theoretical work predicted that a silicon–

based PV material could be further improved [7], sparking interest for further research and development. However, it was not until the energy crisis of the 1970's that the need for alternative resources to fossil fuels started a slowly growing demand for sustainable, earth–friendly energy sources [1]. This prompted, and still drives, R&D efforts to develop new strategies and processing methodologies to produce more efficient and lower–cost PV materials to be price competitive with fossil–based fuel sources.

Solar cells are the smallest active building block of a PV device. A collection of multiples of these cells, connected in series and parallel, creates solar modules, which are arranged together in an array to form a solar panel [1, 7]. The crucial mechanism by which these solar panels work is the formation of a $p - n$ junction [7]. A *p*–type material creates valence electron deficiencies, referred to as holes, whereas an *n*–type material contributes free electrons. Together these form a $p - n$ junction. At the interface of these materials, there is a separation of charge, which induces an electric field, known as the depletion zone. In a semiconductor, when light strikes the material, and energy is absorbed, an electron is dislodged, creating electron–hole mobility. An electric field causes the electron to move towards the *n*–type material and the hole to flow towards the *p*–type material, a mechanism known as photogeneration of charge carriers. As a result, the separation of charges across this junction creates a potential difference. Connecting this material to an external circuit, allows the charge to travel producing an electrical current that can perform useful work [7].

Not all semiconductors are equally effective in generating useful power from a solar cell, with properties like the energy band gap (E_g) and absorption coefficient differentiating the quality of

the active solar cell layer [7]. The E_g refers to the amount of energy needed to excite one electron from the valence band to the conduction band, while the absorption coefficient describes how far into a material the light corresponding to a specific wavelength can penetrate before being absorbed [7]. These two properties impact the efficiency of the solar cell material (SCE). For context, a SCE of above 10% is economically viable (or efficient enough depending on the region). Figure 1.1a, below, represents the maximum efficiency of the film considering the E_g of the material; the peak (30% efficiency) of the graph is known as the Shockley–Quiesser limit of the PV materials [11]. Figure 1.1b shows how the wavelength and material of choice impact the absorption coefficient of the active solar cell layer [12]. The SCE is also influenced by the charge carrier mobility (electron mobility) and charge carrier lifetime within the solar cell, which influence the rate of recombination (the process by which electrons recombine with holes before they can exit the device as light–generated current). A fast recombination rate greatly hinders the full utilization of the photo–generated carriers and limits the efficiency of the solar cell.

The industry standard for PV cells is currently silicon solar cells, boasting an efficiency of 26.6% at standard NREL conditions, comparing films of the same size and shape [13]. Other semiconductor materials, such as cadmium sulphide, gallium arsenide and cadmium telluride, have found their place on the PV technology map – see Figure 1.2 [14]. The shape of each curve is indicative of the initial discovery of these materials followed by technological improvement and eventual stagnation of the efficiency, which is then succeeded by the rapid discovery of newer materials via investigating different material combinations. This graph highlights the dominance of silicon, but also shows the emergence of next–generation solar technology like Indium Gallium Arsenide (InGaAs), a ternary III–V semiconductor, Cadmium Selenide (CdSe), and Hybrid

Organic Inorganic Perovskites (HOIPs), the latter of which is the focus of this thesis. The growth of HOIP materials' efficiency as solar cells in recent years has been staggering; it has grown from less than 4% in efficiency in 2009 and currently lies at over 22% for a single cell [14]. And in December 2018, Oxford PV reported a 28% efficiency for a perovskite–silicon tandem cell [15]. HOIP materials could eventually outperform silicon–based solar cells [14, 16–22]. This thesis is dedicated to understanding the in–solution processes that will ultimately govern the performance of these materials when processed into thin films.

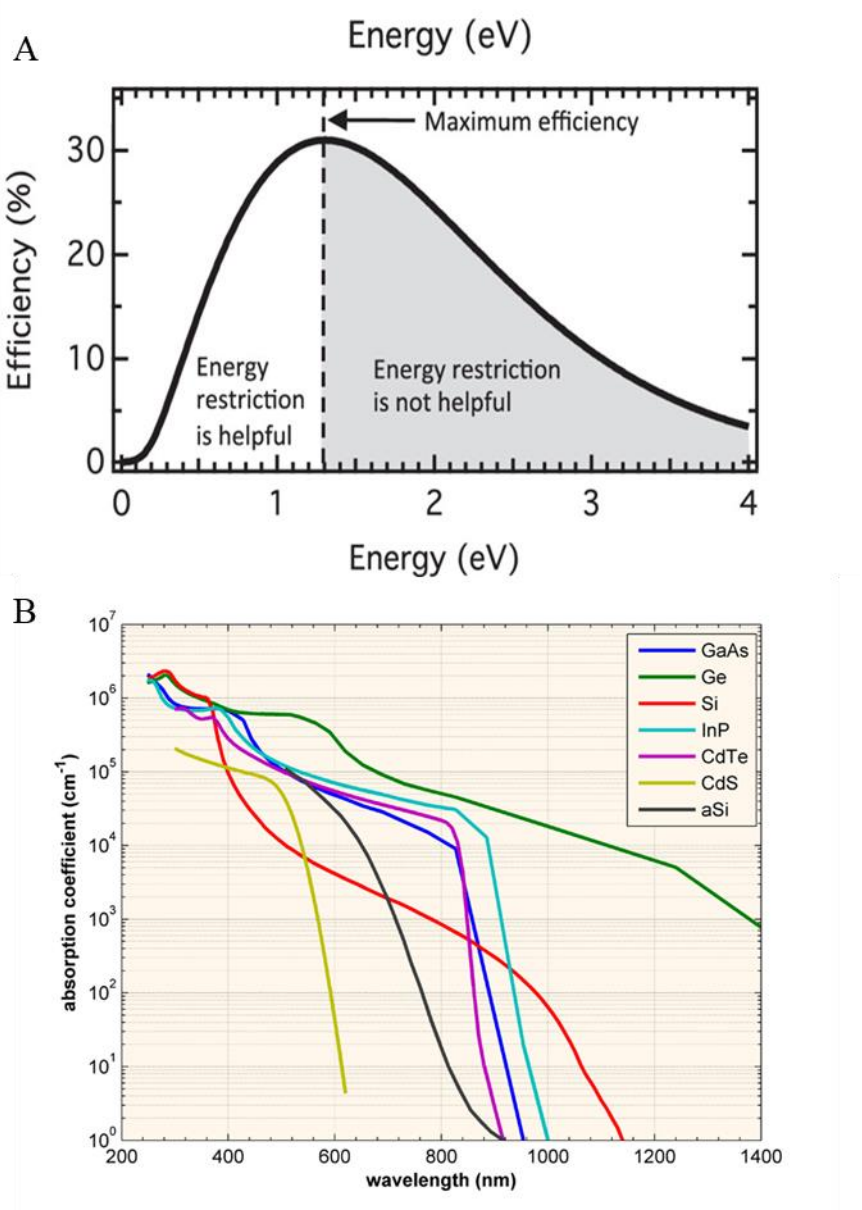

Figure 1.1: a) Energy Band Gap (E_g) versus the efficiency of the PV material; maximum efficiency at around 1.4 eV is known as the Shockley–Quiesser limit used with author's permission [11]. **b)** Wavelength of the light penetrating the PV material versus the absorption coefficient, a measure of how far the light travels before being absorbed by the film used with author's permission [12].

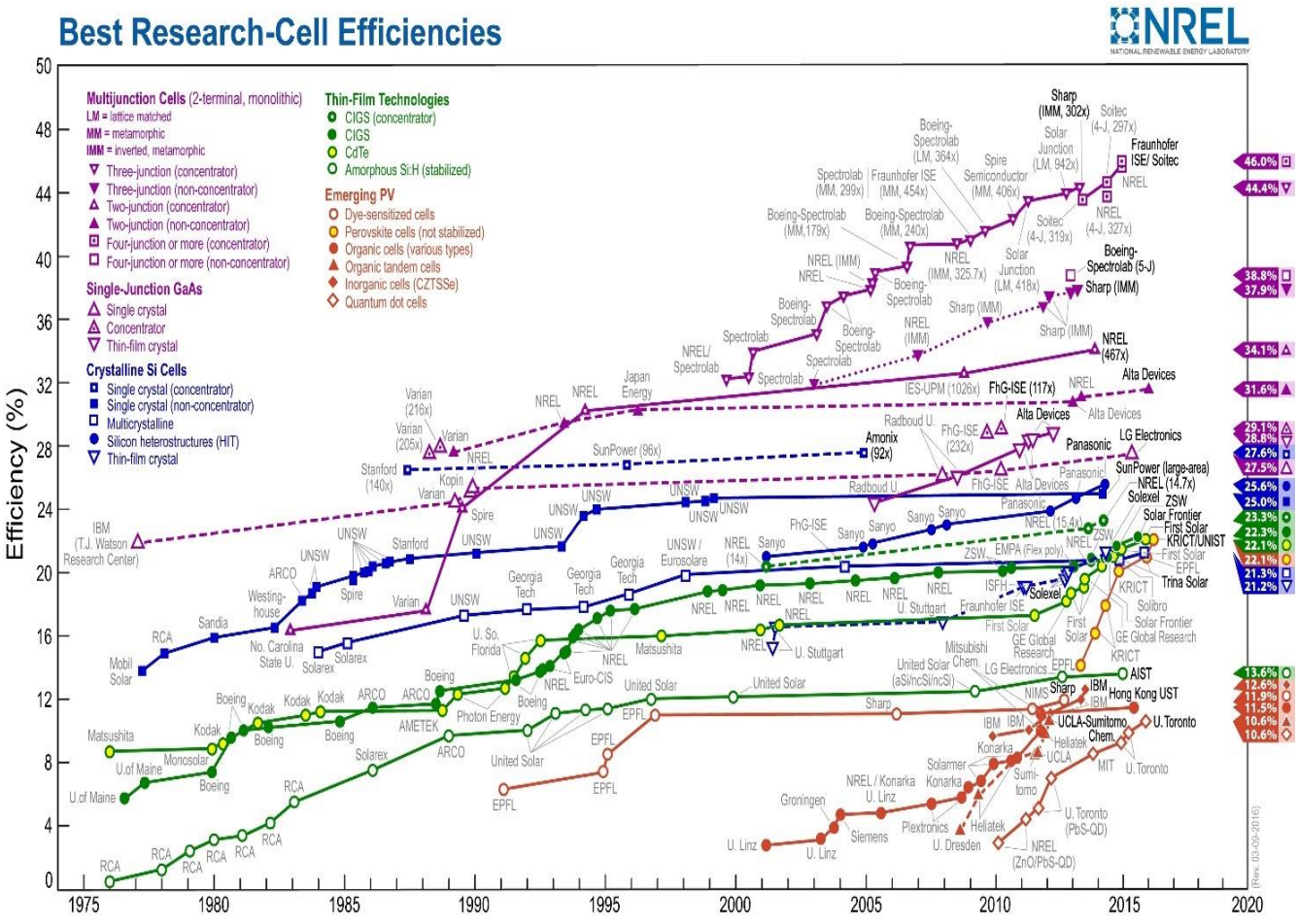

Figure 1.2: NREL diagram showing the growth of various PV technology since 1975 – presented in terms of their improved solar cell efficiency as time progresses [14].

1.2 Hybrid Organic Inorganic Perovskites

Hybrid Organic Inorganic Perovskites (HOIPs) could be a game–changer in solar cell technology if we are to fully transition to renewable technologies. The unique advantage of HOIP materials over silicon lies in the fact these materials can be processed in solution, at room temperature with earth–abundant species, providing a cheap and highly efficient solar cell [16–20, 24–26]. Figure 1.3a shows the National Renewable Energy Laboratory's ranking of the improving solar cell efficiency of HOIPs compared to that of crystalline Si–cells over the past eight years. It shows that HOIP solar cells gained rapidly in efficiency and are more competitive with crystalline silicon cells whose efficiency has essentially plateaued.

Perovskites describe a large class of materials that possess a general chemical formula of ABX_3, where A and B represent different cations, and X is an anion (a halide in the case of HOIPs). Since we are, in principle, able to tailor the choices of A, B and X, this presents thousands of possible candidate material options, by altering the choice of the B–site cation (typically Pb and/or Sn); three choices for the A–site, cation – methyl ammonium (MA), caesium (Cs), formamidinium (FA), and three choices of anion (chloride (Cl), bromide (Br), and iodide (I)) [20, 25]. Figure 1.3b shows the HOIP structure, highlighting the positioning of the A, B, and C–site ions in these materials. These combinations of A, B, X are coupled with over a dozen possible solvents invariably combined into binary blends, adding further complexity to the composition of the solution. Solvent engineering has been experimentally proven to heavily influence the growth and properties of HOIPs from solution, despite yielding identical crystal structures [27–30]. There are simply far too many options to investigate using current experimental or computational

methods. Moreover, there are also different ways to prepare these films – but the most effective HOIP processing techniques have relied on solution processing [31, 32].

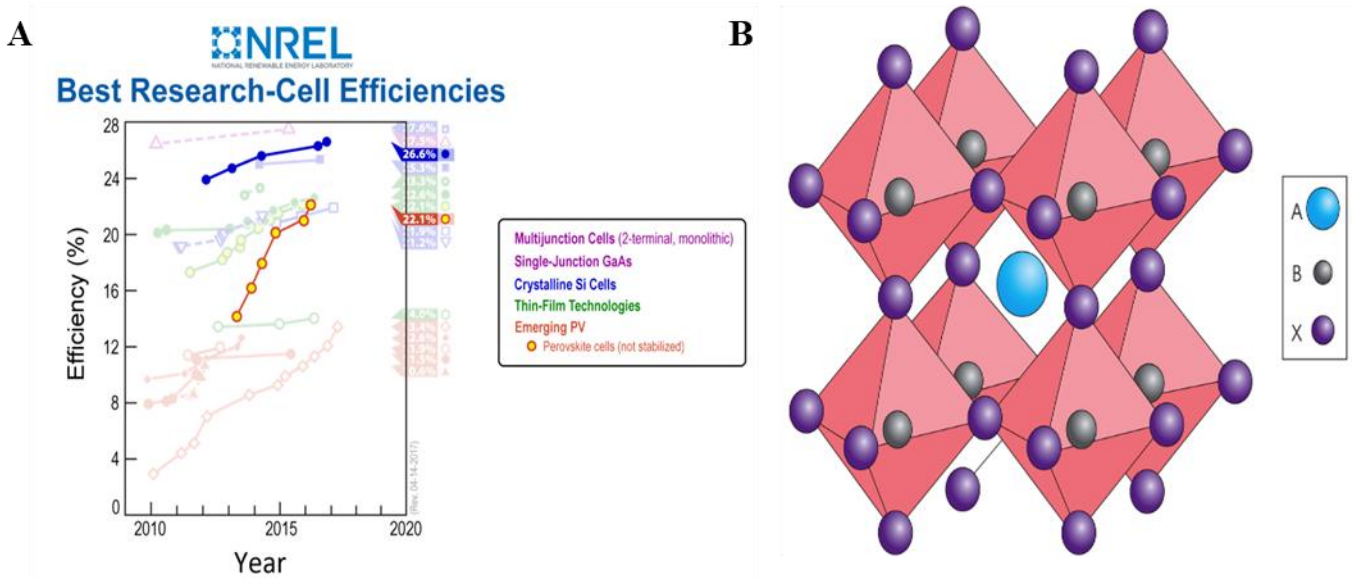

Figure 1.3: a) A close–up on the competition between HOIPs and Crystalline Si cells, produced by NREL [14]**. b)** Structure of HOIPs showing the position of the A, B site cations and the X halide used with author's permission [20].

1.3 Solution Processing of Hybrid Organic–Inorganic Perovskites

HOIP thin films are invariably made in solution using one of two methods or protocols: either a one–step or a two–step preparation. The one–step approach is more common in the literature and involves the simultaneous dissolution of organic and inorganic salts in a polar solvent [29, 32]. In the two–step approach, however, the inorganic salt – being more insoluble – is fully dissolved first to form a solid film, then the organic salt is added. The two–step method has been shown to be a more effective way of preparing the perovskite [31, 33–39]. In both methods, dissolution of the salts is followed by deposition and spin coating of their solvent–salt solutions on a substrate (typically TiO_2) [32]. The crystallization of HOIPs can be described as a two–stage process consisting of nucleation, followed by subsequent growth. In this system, both homogeneous and heterogeneous nucleation events are present, with the former indicative of nuclei formation in the bulk solution and the latter extant at the substrate–solution interface [40]. The driving phenomenon behind the nucleation of HOIPs *via* the one–step method is the degree of supersaturation in the solution mixture, stipulating that the rate at which nuclei form in solution and on the surface, is a function of the rate of solvent evaporation [41]. This relationship has guided techniques such as thermal annealing [42–46], anti–solvent treatments [47–50], and the introduction of system additives (such as HI and HCl) [51–53] to increase the rate of nucleation and growth in the system [41]. Figure 1.4 showcases the experimental controls associated with the preparation of the $PbMAI_3$ perovskite, the combination with the highest reported efficiency (22%). Despite the implementation of these approaches, however, the morphology of the final film is still very sensitive to the choice of solvent used. The HOIP community is now focused on controlling the rate of nucleation (and its subsequent growth) by investigating how the type of

solvent impacts the quality of the film produced as a result of the fabrication process [54–56]. This highlights the current drawback to this technology: the limited understanding regarding how film precursors form the desired thin film HOIP in solution. This lack of knowledge has been attributed as one factor that has limited the commercialization of HOIP technology [19, 30].

To address this issue of solvent effect on thin film quality, current experimental research relies on trial–and–error searches for solvent–precursor combinations and processes that produce highly efficient and relatively stable solar cell devices. However, since early–stage growth from solution controls the quality of the resulting thin film material, outlining the overall crystallization mechanism would help to guide the discovery of effective controls to produce large HOIP crystals with a low density of grain boundaries and defect free morphologies, improving the final film performance [54]. Moreover, understanding the mechanism by which species come together in solution to form the building blocks of perovskite crystals will provide insight into why certain HOIP combinations perform better than others by revealing critical phases of the crystallization process that heavily influence the morphology of the final film. Current experimental attempts to study the nucleation and growth stages have focused on identifying intermediate phases formed during growth through spectroscopic techniques, missing out on the key features driving the growth of these species [57–64]. This provides the opportunity for molecular simulations of the nucleation process in solution to play an invaluable role. Simulations can, in principle, provide a detailed account of the nucleation process, identifying not only its key players/features, but also the dynamics governing the transitions in this system, by studying this process over much smaller time and length scales. Our objective is to "unpack" the solvent effects on these systems using

molecular–scale simulation, which would help to discover the dynamics and features that guide the crystal growth of HOIPs.

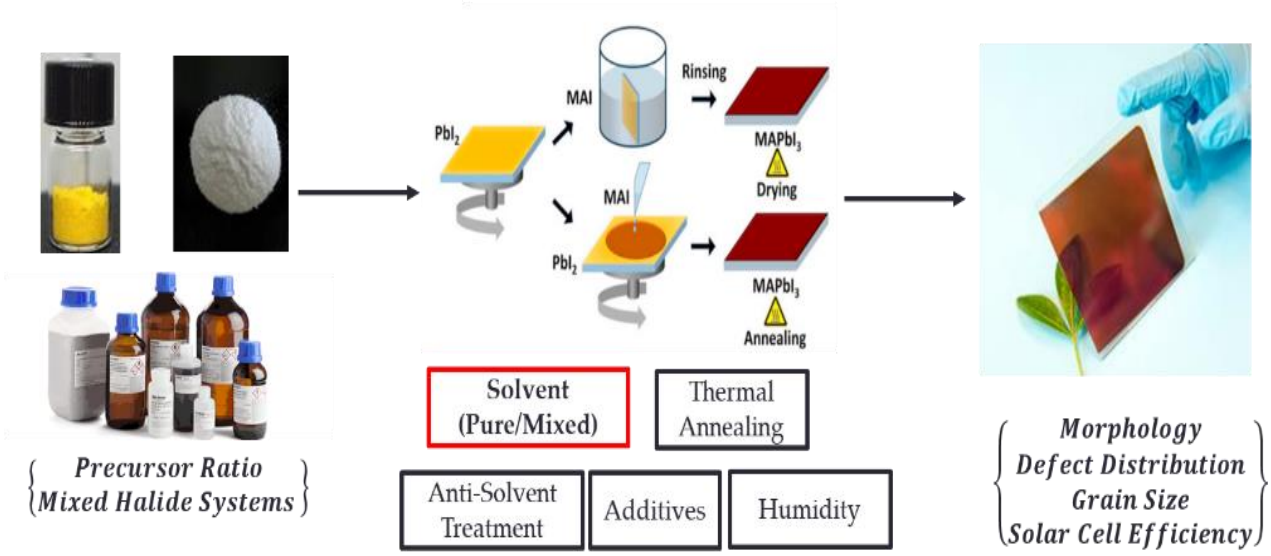

Figure 1.4: Solution Processing of MAPI($PbMAI_3$) combination, emphasis made on the solvent as a means of improving the morphology.

CHAPTER 2

ELUCIDATING SOLVENT EFFECTS ON THE SOLUTION PROCESSING OF LEAD HALIDE PEROVSKITES USING SIMULATION

2.1 Past Computational Studies on Lead Halide Perovskites

The impact of the solvent on the processing of HOIPs has been investigated computationally [56, 65–67]. Figure 2.1, below, showcases the benefits of using computational approaches to study the formation of these materials: we have the advantage of studying how the small–scale species presented impact the final film properties. In this thesis, we will uncover the nature of the iodoplumbates, solvated complexes, and the 'monomers' or nuclei that will ultimately combine to form the HOIP crystal, that are formed from the solution process. As mentioned above, solvent engineering is of great importance in enhancing the morphology and final film solar cell efficiency of these materials, and recent studies and publications have highlighted the importance of this stage in the fabrication of HOIPs [54, 55, 57].

Such studies have focused on providing metrics to evaluate solvent efficacy and subsequently suggesting solvent alternatives to the current commonly used "standard" solvents, DMSO and DMF [22–33, 65, 68–77]. Experimental metrics like Gutmann's donor number (D_N) [55], and computational metrics like the Unsaturated Mayer Bond Order (UMBO) [65] have predicted the efficacy of DMPU and THTO, respectively, as alternatives towards achieving higher quality films

by delaying the nucleation of the perovskite crystal. Both the D_N and UMBO are explained in detail later in this thesis [55, 58, 77].

Earlier posited metrics, such as the Hansen solubility of the solvent have fallen out of favour [65]. Computational studies have gone beyond simply providing metrics; they have also predicted the favourability of certain solvent–cation pairs during perovskite formation. For example, Cao *et al.* showed that the DMSO – MAI interaction is more favourable than DMSO – FAI, with the former leading to the formation of better films *via* a more stable solvent–salt adduct [56]. In addition, Herbol *et al.* recently used Bayesian Optimization–based machine learning techniques to identify favourable combinations of cations, anions, and solvents that are predicted to lead to improved film performance based on the interaction energies (binding energy) between a solvent and 'monomer' [66]. Moreover, molecular simulations have also been used to suggest pathways for nucleation and growth of the perovskite from its precursors (PbI_2 and MAI) in a GBL solvent environment [67]. This paper by Ahlawat *et al.* outlined the different stages of nucleation and growth and relevant species, cluster orientations, and interactions that play a role in the growth of the perovskite film. Overall, computational studies of these systems have complemented experimental efforts not only by providing the atomic details of the key moieties and features in solution, but also the dynamics governing the transitions from reagents to precursor to perovskite units in these systems. This is achieved by studying the process over much smaller time and length scales.

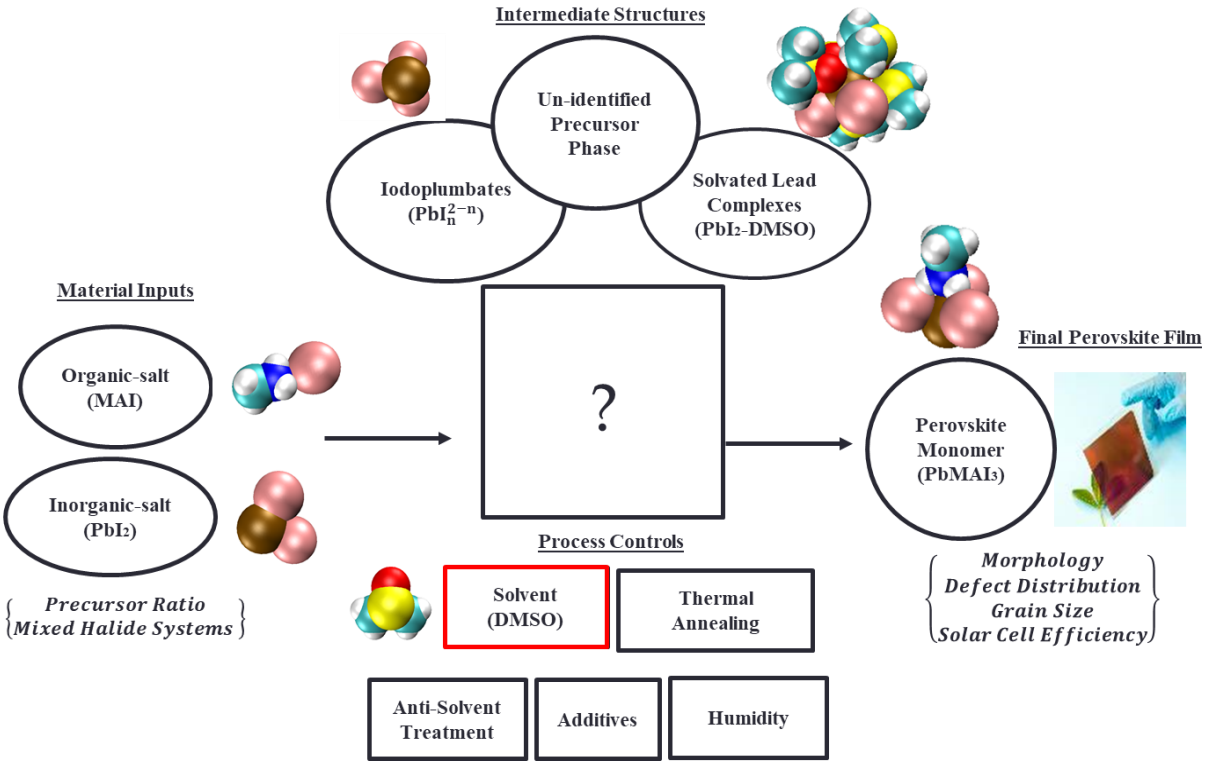

Figure 2.1: Species and structures relevant in the solution processing of MAPI perovskites, namely, inorganic–organic salts, iodoplumbates, solvated complexes, an unknown precursor phase with solvent and halide coordination to PbI_2, and the repeating MAPI unit (monomer). The empty box at the center of the image hints at the lack of understanding of what happens in this solution process.

2.2 Simulation Details

Molecular simulation studies allow us to look at the mechanistic details of large–scale reactions and identify key atoms and molecules playing a role in the processes. Figure 2.2 compares different simulation methods based on their accuracy/detail, the time scales over which these results are obtained, and the computational cost (generally measured in CPU hours) to run these simulations. Two simulations methods are discussed in this thesis: Molecular Dynamics and *ab initio* (Density Functional theory) calculations.

2.2.1 Molecular Dynamics (MD)

MD is a computational technique that simulates the motion of atoms and molecules in time and space giving a representation of the dynamical evolution of the system. MD numerically solves Newton's (or other) laws of motion, as a means to calculate the trajectories of particles as they evolve through space and time. Any forces of attraction or repulsion acting on the particles and their relevant potential energies are represented by force fields, which are mathematical models that describe short–range and long–range interactions between atoms and molecules [78, 79]. Popular examples of force fields include Optimized Potentials for Liquid Simulations (OPLS), developed originally by Jorgensen *et al*. [80, 81], which describes intramolecular interactions within molecules by specifying bond, angular, and dihedral parameters and the Lennard–Jones (LJ) and Coulombic potentials, describing the intermolecular interactions between neighboring molecules. MD techniques were originally developed in the late 1950s; since then it has become

very popular in fields like chemical engineering, materials science, chemistry and chemical physics, and biological engineering [80].

2.2.2 *Ab initio*, Density Functional Theory (DFT) Calculations

Going further up in accuracy (and smaller in scale) are *ab initio* techniques like DFT, [82–85] based on Schrödinger's fundamental principles of electron configurations and interactions. When the Schrödinger equation was developed in 1926 [86], it provided the means to determine the electronic and nuclear ground–state energy of a system of atoms, hence characterizing the Potential Energy Surface (PES) [87]. Since the PES can only be solved exactly for one electron, methods such as DFT were created to approximate the ground–state energy of a system of many, interacting electrons using quantum mechanics [88].

DFT iteratively solves the wave equation of the electron system in terms of an electron density functional until a pre–specified convergence in energy has been reached. The wave equation is solved *via* the Schrödinger equation with the appropriate Hamiltonian. The electron density functional is a mathematical formulation approximating the spatial dependence of electron density; efforts are still being made to improve the accuracy of electron density functionals [89–92]. DFT has become a very popular choice of method to approximate the energy of a system of atoms [93–98]. DFT calculations in this thesis were performed using the ORCA software package [99], which provides basis sets for approximating molecular orbitals and electron density functionals. The governing interactions between electrons need to be specified and are sensitive to the basis sets and density functionals [100]. Alhrichs' def2–TZVP was selected as the basis set for this thesis, which is known to be effective for converging energies [99, 101–103]. We used

the B97–D3 functional (a Generalized Gradient Approximation (GGA) functional [104, 105]), recommended for its performance as well as the PW6B95 functional [106, 107].

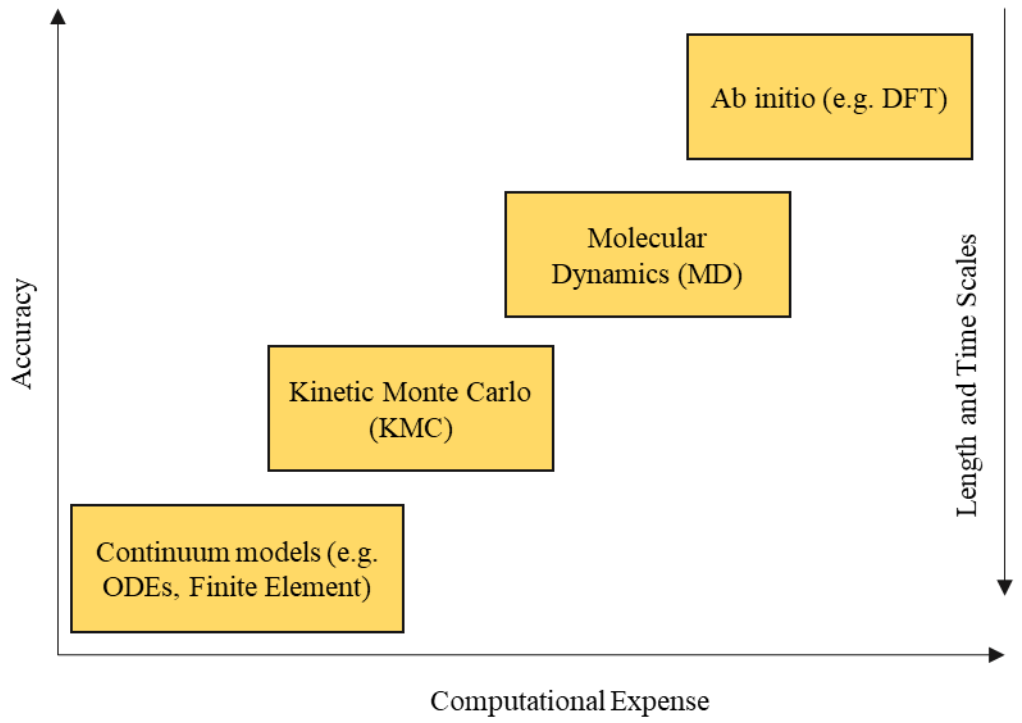

Figure 2.2: Relationship between the "accuracy" (or perhaps scale or resolution) of various molecular modeling methods with their computational cost. The more accurate the approach, the more computationally expensive it is to make calculations of energies and thermodynamic properties.

2.3 Metric Studies

Our first approach into understanding the influence of solvent choice on HOIP production involved investigating which among the various physico–chemical features of solvents are indicative of whether they will make good candidates for the preparation of high–quality MAPI films. Solvents differ in properties such as partial charge distribution, size, and the extent of saturation within their bonds, which influences their affinity for certain species or reagents.

In PbI_3MA perovskites, a key element involves the dissolution of the lead salt (PbI_2) [31]. We have investigated the solvation of the lead salt, in six solvents of interest: Dimethyl propylene–urea (DMPU), dimethyl sulfoxide (DMSO), N–methyl–2–pyrrolidone (NMP), N, N–dimethylformamide (DMF), γ–butyrolactone (GBL), and propylene carbonate (PC). The structure of the solvents and their Gutmann Donor Number (D_N) are as outlined in Table 2.1 below. Employing the D_N allowed us to categorize solvents with the highest D_N (DMPU, DMSO) as 'strong' solvents, solvents with median D_N (NMP, DMF) as 'moderate' solvents (forming a complex of adequate strength) and solvents with the lowest D_N (GBL, PC) as 'poor' solvents that form relatively weaker complexes when bound to the central Pb atom of the PbI_2 molecule (the Pb^{2+} center). Our objective was to probe the structural/geometric, electronic, and bond saturation features of the complexes formed from these six solvents to reveal why certain solvents perform better than by comparing these properties to the D_N metric [55, 108, 109].

Solvent	Donor Number (kcal/mol) [55]	Structure	VMD Image	Grouping
DMPU	34	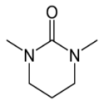	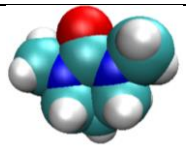	Strong Solvents
DMSO	30	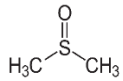	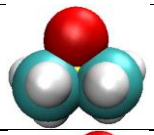	
NMP	27		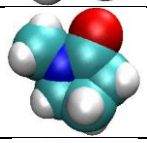	Moderate Solvents
DMF	27		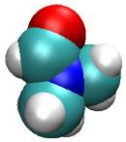	
GBL	18		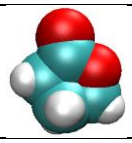	Poor Solvents
PC	15	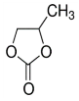	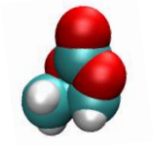	

Table 2.1: Showing the solvents selected for this metric comparison study: Dimethyl propylene–urea (DMPU), dimethyl sulfoxide (DMSO, N–methyl–2–pyrrolidone (NMP), N, N–dimethylformamide (DMF), γ–butyrolactone (GBL), propylene carbonate (PC). Color scheme for Visual Molecular Dynamics (VMD) images: Oxygen (●), Sulfur (●), Carbon (●), Hydrogen (●), Nitrogen (●), Lead (●), Iodide (●).Classification of solvents as Strong, Moderate, and Poor was based on their Gutmann Donor Number values.

2.3.1 Gutmann's Donor Number

Gutmann's donor number (D_N) is an experimental property used as a metric to represent the hardness/softness of a base towards antimony pentachloride ($SbCl_5$) in a dichloroethane solvent medium. The hardness of an acid (in this case Sb^{5+} in combination with a base) with a given solvent was measured using this metric and its results are consistent with the underlying 'hard' and 'soft' (Lewis) acids and base (HSAB) theory it is based on [109, 110]. This theory suggests that harder acids form stronger complexes with harder bases, likewise softer bases form stronger complexes with softer acids; the hardness or softness of an acid or base is determined by the size of the donor atom, its charged state, and polarizability [109, 110].

The D_N was first suggested by Yoa *et al.* [108] and further supported by Hamill *et al.* [55] in their papers showcasing its effectiveness at predicting the solvation of PbI_2. The formation of the 1:1 complex formed between a solvent, B, and $SbCl_5$ at 298 K in a dilute solution of 1,2–dichloroethane is represented in Figure 2.3. The D_N, or Lewis basicity, is determined by the enthalpy difference between Equations 2.1 and 2.2, *i.e.*, ΔH (Equation 2.2) – ΔH (Equation 2.1).

$$B(pure) \rightarrow B(solution) \tag{2.1}$$

$$B(pure) + SbCl_5(solution) \rightarrow B\text{–}SbCl_5(solution) \tag{2.2}$$

One drawback to this metric is that DN values are not readily available. Current D_N values have only been reported for oxygen bases – mainly carbonyl compounds – and a few nitrogen, carbon, and halogen bases [109, 110]. Data for the D_N of the six solvents are included in Table 2.1.

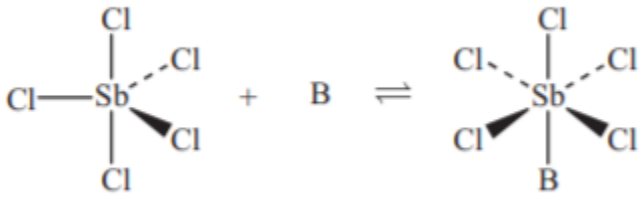

Figure 2.3: Key interactions in the determination of Gutmann's donor number: Here B represents the choice of solvent molecule; while Sb and Cl are the elemental symbols for antimony and chlorine, respectively. The result is a $SbCl_5$–Solvent/Base complex formed between $SbCl_5$ and solvent (B) [110].

2.3.2 Computational Metric Evaluations

Given that the D_N involves a non–trivial experimental determination and hence values are not available for all the solvents of interest to the community in HOIP processing, we set out to provide metrics that correlate well with the D_N, and which could be determined readily from a computational route. The availability of such a metric would provide a significant savings in time and a resource/opportunity cost advantage over experimental measurements needed to determine the D_N. This study could also be useful in uncovering the features of the solvent–solute interactions that influence macroscopic properties, like the rate of nucleation and cluster size, observed *via* experiments.

To determine alternative solvation metrics, we compared the D_N to the density functional theory features of solvated lead complexes for each of the six solvents outlined in Table 2.1. These solvated complexes involve four identical solvent molecules *(i.e.*, for a pure solvent) coordinating to the Pb^{2+} center of a PbI_2 molecule. A coordination number of 4 was selected because Pb^{2+} prefers to make, at most, six bonds as suggested by VSPER theory [111] – see Figure 2.4. In the case of PbI_2, two of these bonds are satisfied by bonding to iodine atoms, although Stevenson *et al.* have shown that a solvent coordination number greater than four is possible [65]. This fully solvated complex was then optimized in DFT using a particularly accurate double–hybrid functional (B97–D3) and an accurate triple–zeta basis set (def2–TZVP). From these DFT calculations, we determined structural, charge, and enthalpic information by looking into the binding energy, UMBO of the formed complex, the solvent and halide coordination distances to the Pb^{2+} center, and charges around each molecule associated with the formed structures. All

charges represented are CHELPG charges [112]. In the subsections below, we investigate the usefulness of several different metrics to correlate with the D_N.

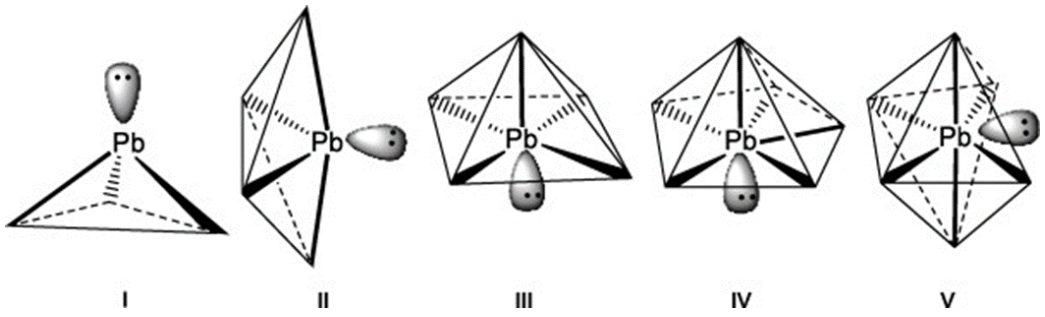

Figure 2.4: Pb^{2+} complex structures suggested by VSEPR theory for different numbers of complexing groups (3–8 from left to right). Figure from Davidovich *et al.* [111], used with the authors' permission.

2.3.2.1 Metric 1: Interpretation of Enthalpic (Binding Energy) Results

Binding energy (BE) calculations, determined using the Equation 2.3 below, are used since they are known to reveal information about the enthalpy of the PbI_2–solvent complexes and rank their relative stability or metastability [65, 77]. This involves determining the energy of three separate systems that will be simulated in this thesis: solvent alone, solute alone, and the solute–solvent complex. Equation 2.3 and Figure 2.5 are complementary and depict the determination of the binding energy of the PbI_2 – 4DMSO complex, where the four indicates that four solvent molecules were bound to the lead salt.

$$\Delta E_{binding} = E_{Solvated\ Complex} - E_{nSolvent} - E_{PbI_2} \tag{2.3}$$

Binding energies for the solvated complex correlate well with the reported values of the D_N (experimental observations) for these solvents (see Figure 2.6). These enthalpic results identified the single solvent–solute interaction with the largest (most negative) binding energy result as that belonging to DMPU, followed by DMSO – the solvents with the highest D_N values – as shown in Table 2.1. Figure 2.6 also revealed that solvents with lower D_N values, like PC and GBL, also bind less strongly to Pb^{2+} center than solvents with a higher reported D_N [108].

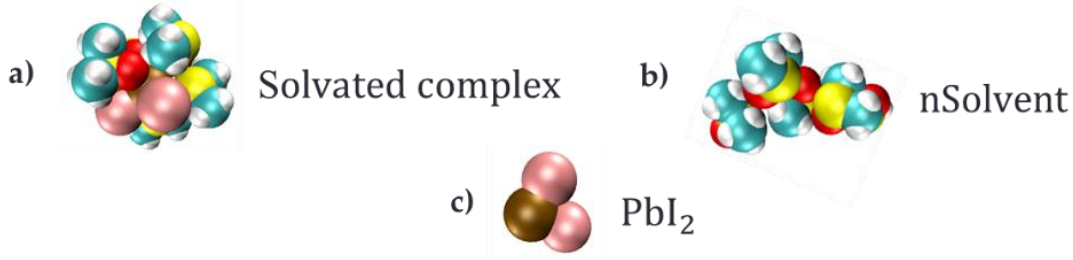

Figure 2.5: Pictorial representations of (a) a solvated complex of n solvent molecules bound to PbI_2; (b) *n* solvent molecules (in case 'a' and 'b', n = 4); (c) the PbI_2 solute. Color scheme as shown in Table 2.1.

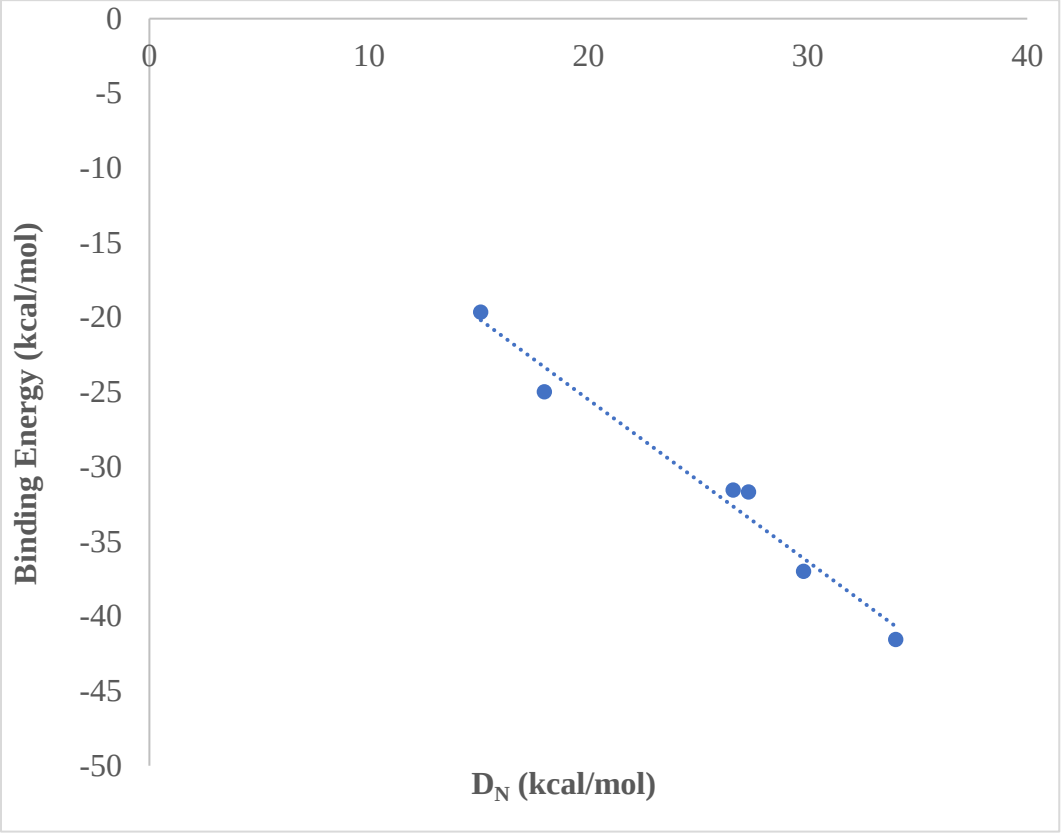

Figure 2.5: Correlation between binding energy (BE) and the D_N (R^2 = 0.97), where the six data points represents results for the six chosen solvents listed in Table 2.1.

2.3.2.2 Metric 2: Interpretation of Structural Results

We obtained structural information from the distance between the Pb^{2+} center and the solvent molecules, distances between Pb^{2+} center and iodide atoms, and geometric data of the six solvent molecules making up each complex, as discussed in the subsections below. The coordination distance was measured by calculating the distance characterizing the dative bond formed between the Pb^{2+} center and the 'O–' donor solvent (Pb–O). Pb–iodine distances were determined by calculating the percentage change in the iodide's coordination distance from its simulated value in the absence of solvent (2.92 Å). The solvent's size is represented by the 'minimum volume–enclosing ellipsoid' (MVEE), which approximates the volume of each solvent molecule as an elliptical object, as depicted in the image below (Figure 2.7).

We calculated the average bond distance between the central Pb atom and the bound solvent molecules, as well as the change in the Pb atoms coordination with the two iodide ions, to reveal the coordination distances of the associated [solvent – PbI_2] systems, as shown in Figures 2.8 and 2.9, respectively. We originally hypothesised that more weakly coordinating solvents should coordinate less strongly with the Pb^{2+} center ion and have a smaller iodide coordination distance – indicating a weaker interaction with the Pb atom than the halide ions.

This hypothesis was confirmed, to some extent, in this study, with lower D_N solvents like GBL and PC exhibiting a longer (weaker) coordination distance to the central Pb atom than the other higher D_N solvents in this study, albeit only by a very small distance, 0.2 Å. There is also no linear correlation: low D_N solvents fall into one group at around 2.8 Å and high D_N value solvents clustered around 2.6 Å. This metric, then, is not a suitable choice for a simple representation of the bonding proclivities of the solvent molecules to the Pb^{2+} center ion. However, low D_N solvents

also facilitated closer coordination to the bound halide atoms in comparison to the other solvents (5% lower Pb–I extension than the other solvents). There is a more distinct correlation when comparing the lengthening of the Pb–I distances to the D_N (see Figure 2.9). The higher the D_N, the greater the lengthening of the Pb–I bond, with a roughly linear correlation between the two parameters.

From our investigation on whether there was a correlation between the size of the molecule, as described by the minimum volume–enclosing ellipsoid, and the D_N, the MVEE does not correlate with the donor number (Figure 2.10). There is a possibility that the size of the solvent affects the number of neighboring solvents capable of coordinating with the Pb^{2+} center; the extent of solvent packing and coordination around the solute might influence the differentiation among the effectiveness of certain solvents. However, this was not further explored in this study. Overall, of the tests we made of simple physical characteristics of the bonding around the Pb^{2+} center, we found that the lengthening of the Pb–I bond length provided the best structural correlation with the D_N, implying that strong coordination to the Pb^{2+} center is often accompanied by a lengthening of the halides away from the Pb^{2+} center.

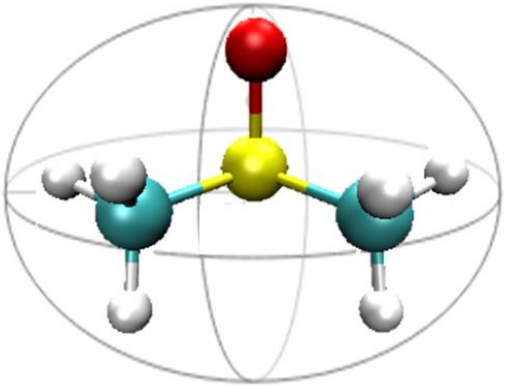

Figure 2.7: Oval representing the minimum volume–enclosing ellipsoid (MVEE), shown here for a DMSO molecule. Color scheme as shown in Table 2.1.

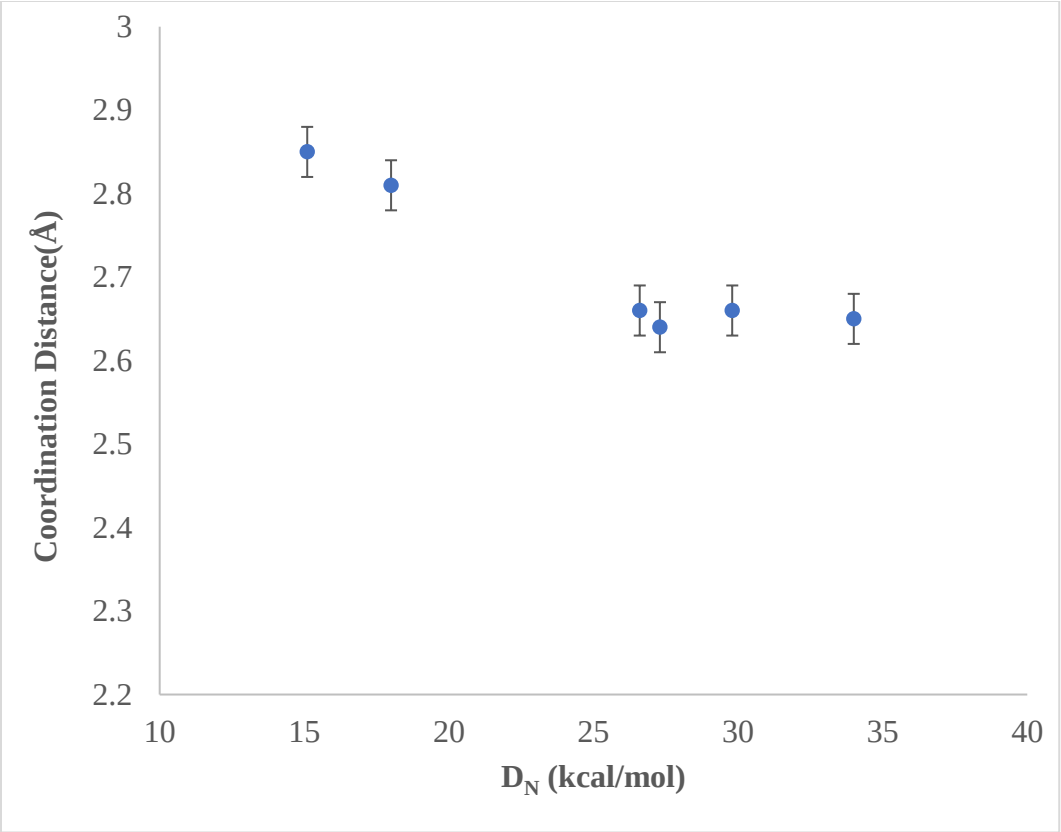

Figure 2.8: Correlation between the D_N and the coordination distances of the bound solvent molecules to the Pb^{2+} center.

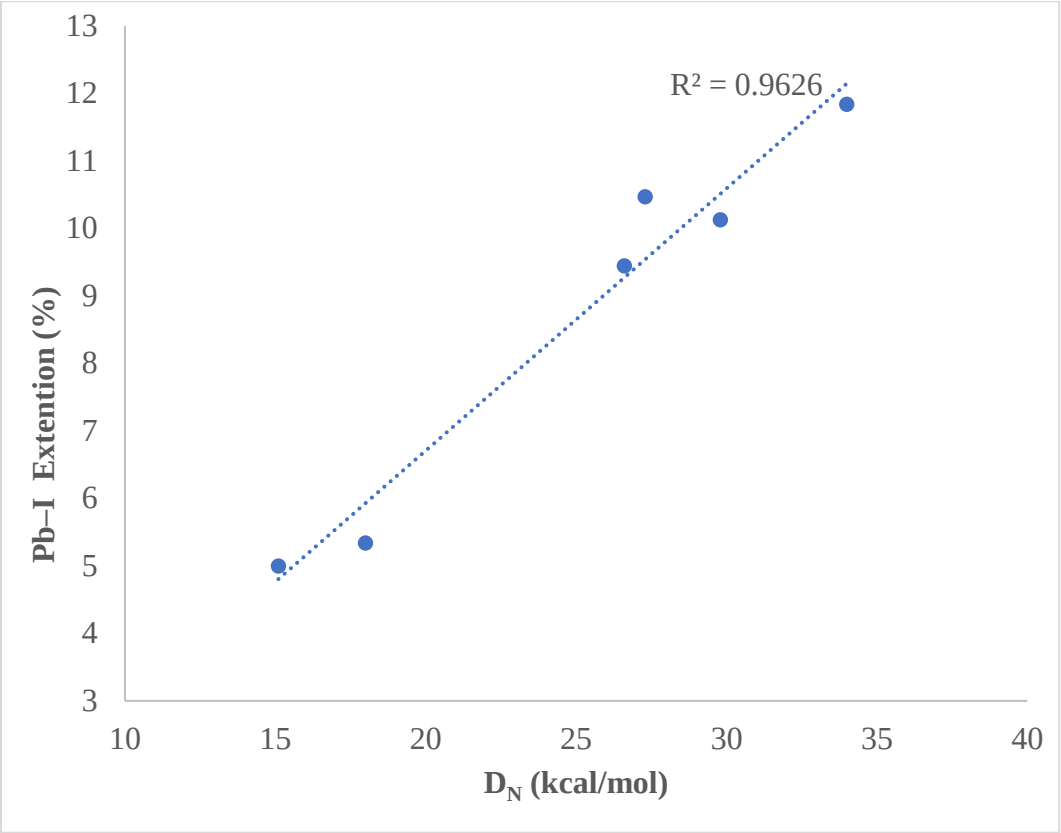

Figure 2.9: Correlation between the D_N and the extension of the iodide coordination distance (*i.e.*, the Pb–I distances), with an $R^2 = 0.96$.

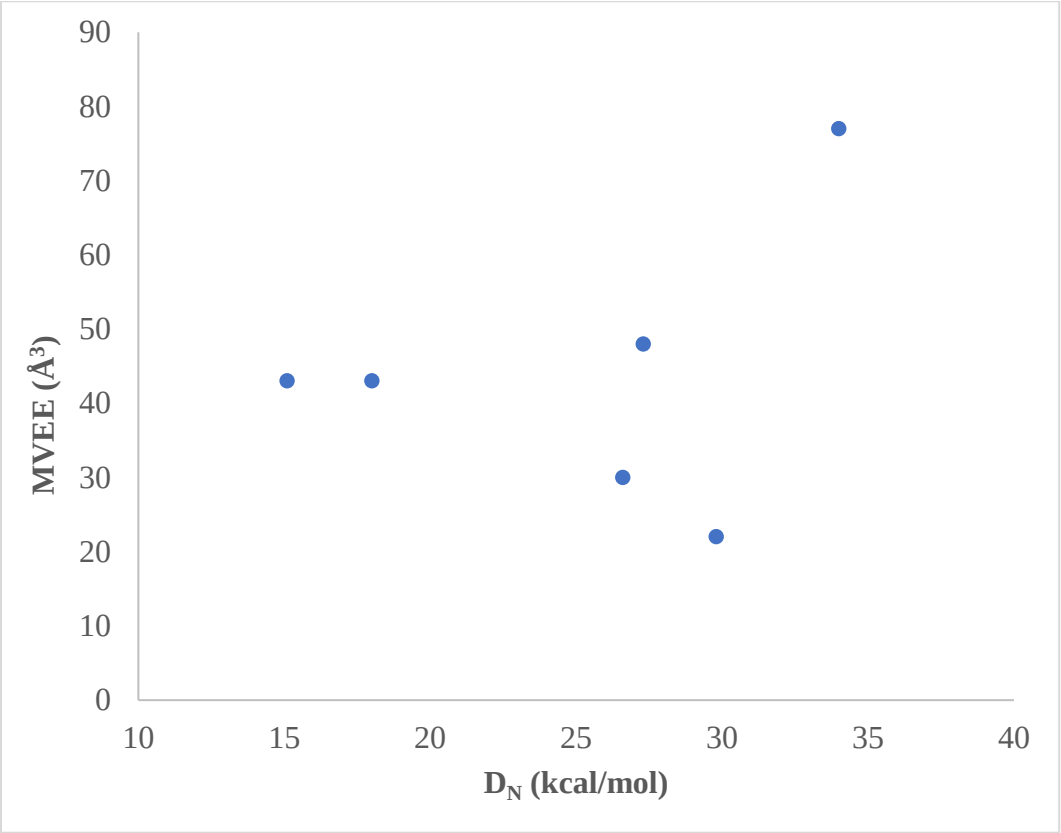

Figure 2.10: Correlation between the D_N and MVEE, the minimum volume enclosing ellipsoid.

2.3.2.3 Metric 3: Investigation of the Correlation between Bond Saturation (MBO and UMBO) and Gutmann's Donor Number (DN)

The Mayer Bond Order is a tool used in computational chemistry to provide useful bonding analysis features (like the electron saturation within a bond) *via* semi–empirical computational methods [113]. It has been successfully used to represent bonding features for a variety of molecules ranging from transition metal complexes to carbon ring structures [113, 114]. We have used the MBO to determine the bond saturation at the more polar end of the solvent molecule (C=O or S=O). For example, the MBO for the C=O bond of DMSO (emphasized in Figure 2.11) is 1.56, whereas the formal bond order of this double bond is 2.0 [115].

The UMBO is an acronym for the Unsaturated Mayer Bond Order. This is a simple construct that quantifies the difference between the formal bond order and the MBO value. Hence, in the example given above for DMSO, the UMBO would be the difference between 2.00 and 1.56 and, hence, would have a value of 0.44. The larger the UMBO, the greater the solubilization of the Pb^{2+} center. As showed by Stevenson *et al.* [65] the MBO (and UMBO) provide a cheap and computational inexpensive tool to assess solvent efficacy by measuring the bond saturation within the bond containing the most polar end of the solvent. Ranking the ability of solvents to solubilize the lead salt using the UMBO has already been validated in comparison to experimental results [65, 77].

In this thesis, we have produced an alternative metric to the UMBO, measuring the reduced electron saturation within a bond (C=O or S=O) when a dative bond between the solvent and solute is formed (Pb–O). As seen in Figure 2.11, the dative bonding between Pb^{2+} and DMSO alters the bond saturation in the C=O bond from 1.56 (observed in the case of a single solvent in

isolation – *i.e.*, the original UMBO) to 1.44, resulting in dissimilar UMBO values. The two UMBO metrics were determined using the B97–D3 functional and show good agreement with the results obtained by others with the PW6B95 functional, which was used in a published paper [65] (see Figure 2.12). This justifies the use of the less computational expensive functional for these calculations.

There was no correlation observed between the D_N and the MBO for the Pb–O bond (the dative bond between the solvent and solute), as seen in the blue data points in Figure 2.13. The MBO for the Pb–O bond remains constant at a value of about 0.18. However, there is a more indicative trend observed between the Pb–I bond order (red points in Figure 2.13): the smaller the MBO, the larger the D_N. This observation suggests that stronger solvent interactions (from a higher D_N solvent) is not reflected in the electron saturation within the newly formed bond between the solvent and Pb^{2+} center. Instead, this interaction alters the saturation within the already formed bond between the cation and halide. This reduced saturation, with higher D_N, also hints at how the solvent molecule effectively solubilizes the lead salt through weakening the interaction between the Pb^{2+} center and its bound iodide ions [116].

There is also a weak correlation between the D_N and the UMBO (R^2 = 0.55), but this trend improves when comparing the D_N with the UMBO of the complex (R^2 = 0.79), see Figures 2.14 and 2.15. The improved trend with the UMBO of the complex to the D_N suggests that the electron saturation in the polar end (C=O or S=O) of the solvent molecule becomes less saturated as the binding propensity increases. Overall, both UMBO metrics can identify the higher–ranking D_N solvents (DMPU and DMSO), middle ranked D_N solvents (DMF and NMP), and lower ranking D_N solvents (GBL and PC).

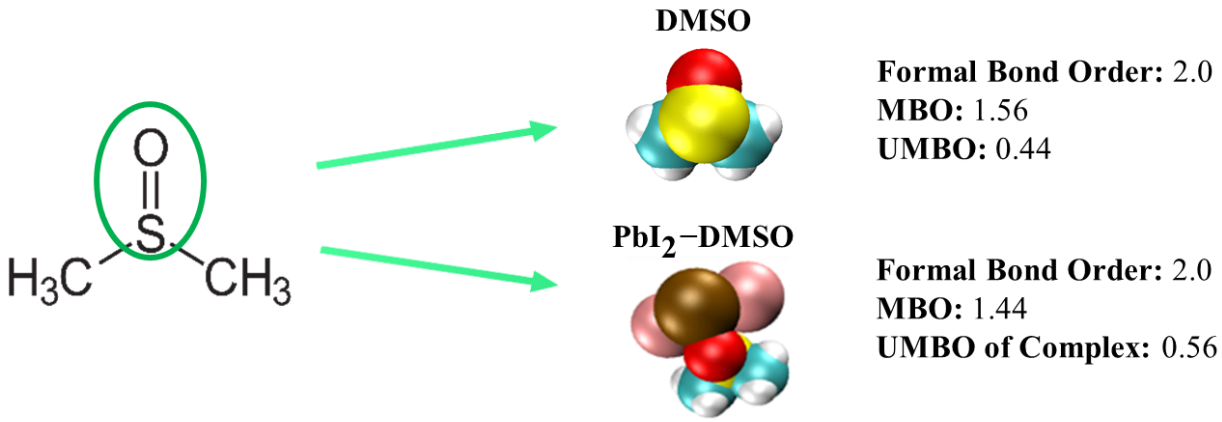

Figure 2.11: A pictorial and numerical determination of the MBO, UMBO (Single DMSO Solvent), and UMBO of the complex (PbI_2–DMSO). Color scheme as in Table 2.1.

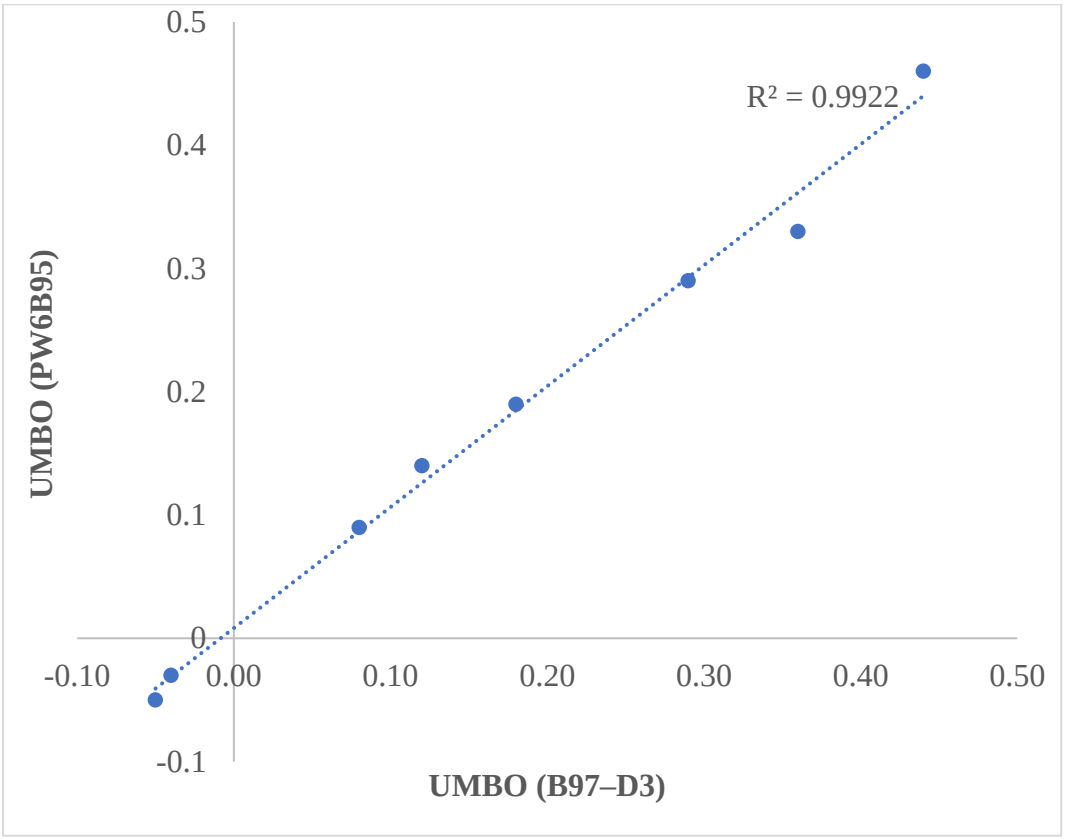

Figure 2.12: The UMBO calculated using the B97–D3 functional is sufficiently accurate for UMBO calculations; there is a strong agreement with the UMBO calculated using the PW6B95 functional, with an $R^2 = 0.99$.

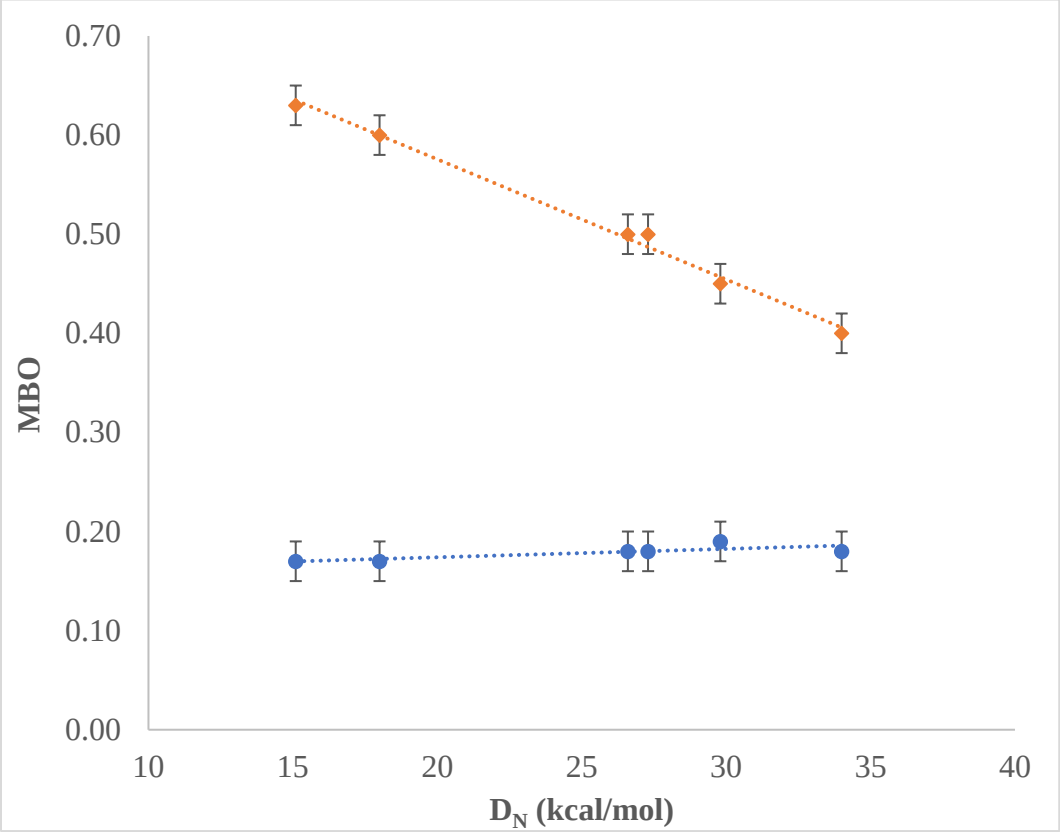

Figure 2.13: Mayer Bond Order of Pb–O (●) (R^2= 0.65) and Pb–I (♦) (R^2 = 0.99) bonds garnered from ORCA DFT simulations of PbI_2–4Solvent complexes in comparison to the D_N.

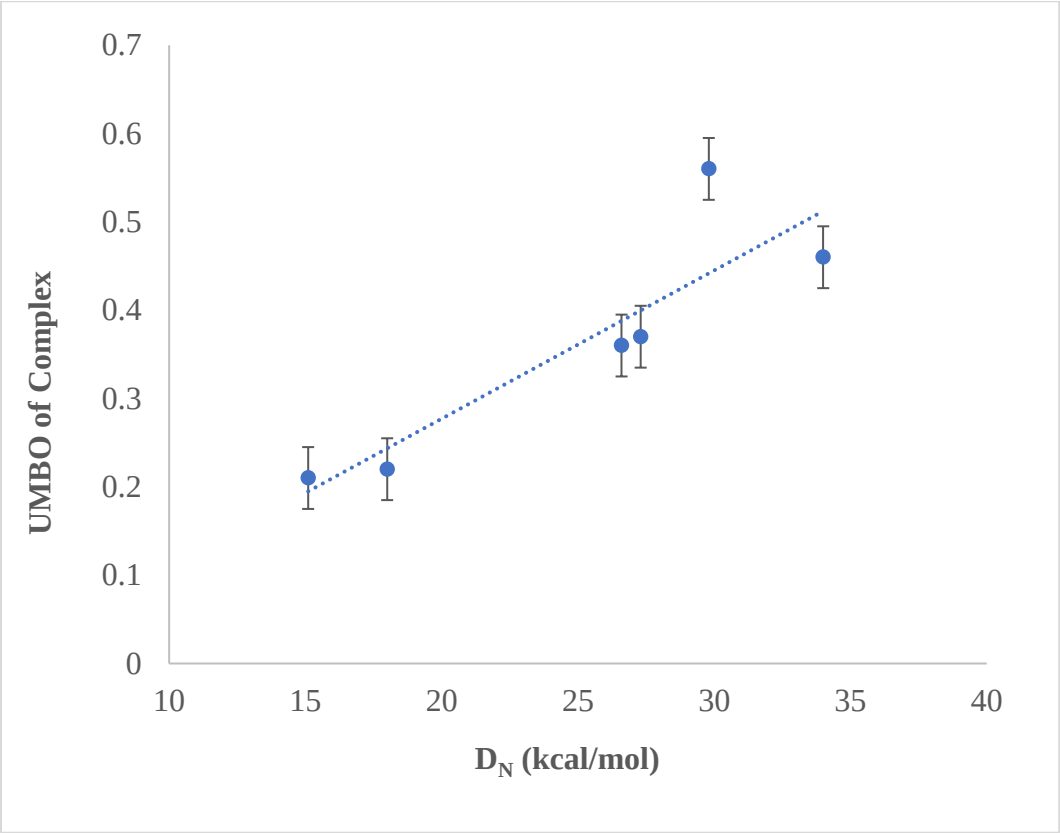

Figure 2.14: Correlation between the UMBO of the complex (solvent molecule bound to PbI_2) and D_N (R^2 = 0.79). Error bars indicate the spread of the UMBO for the four solvents coordinating to the Pb^{2+} center.

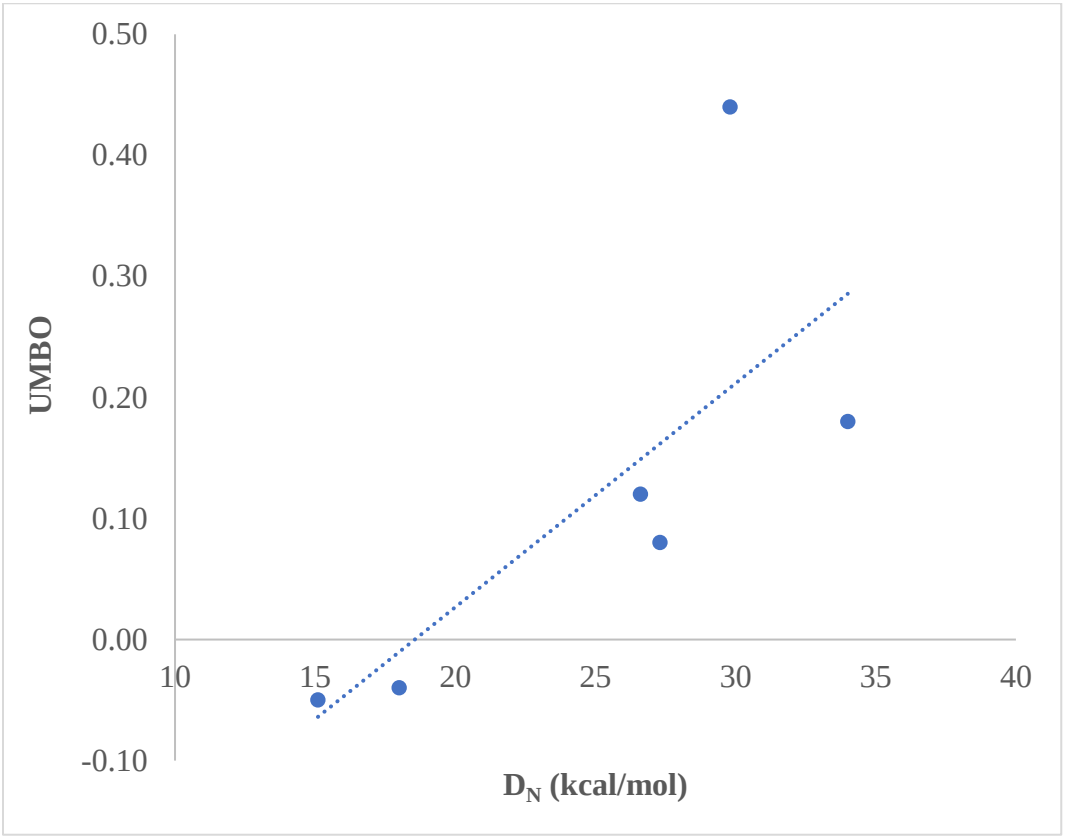

Figure 2.15: Correlation between UMBO (isolated single solvent molecule) and the D_N (R^2 = 0.55).

2.3.2.4 Metric 4: Correlation of Partial Charges with Gutmann's Donor Number (DN)

We first compared the charge of the dative atom ('O', Oxygen) for each solvent to the D_N, which showed no direct correlation with this metric (Figure 2.16), confirming that the charge of this atom does not directly relate to the strength of its interaction with the Pb^{2+} center. So, we decided to investigate how the charge on this end of the solvent molecule compares with the rest of the atoms in the solvent *via* the dipole moment, which was obtained directly from ORCA [104–107]. No correlation between this metric and the D_N was observed, as shown in Figure 2.17, revealing that the polarity, or lack of polarity, is not influencing a solvent's coordination strength to PbI_2 [65]. Moreover, this confirms that the D_N chemistry dictates solvation propensity more so than electrostatic interactions [65, 117].

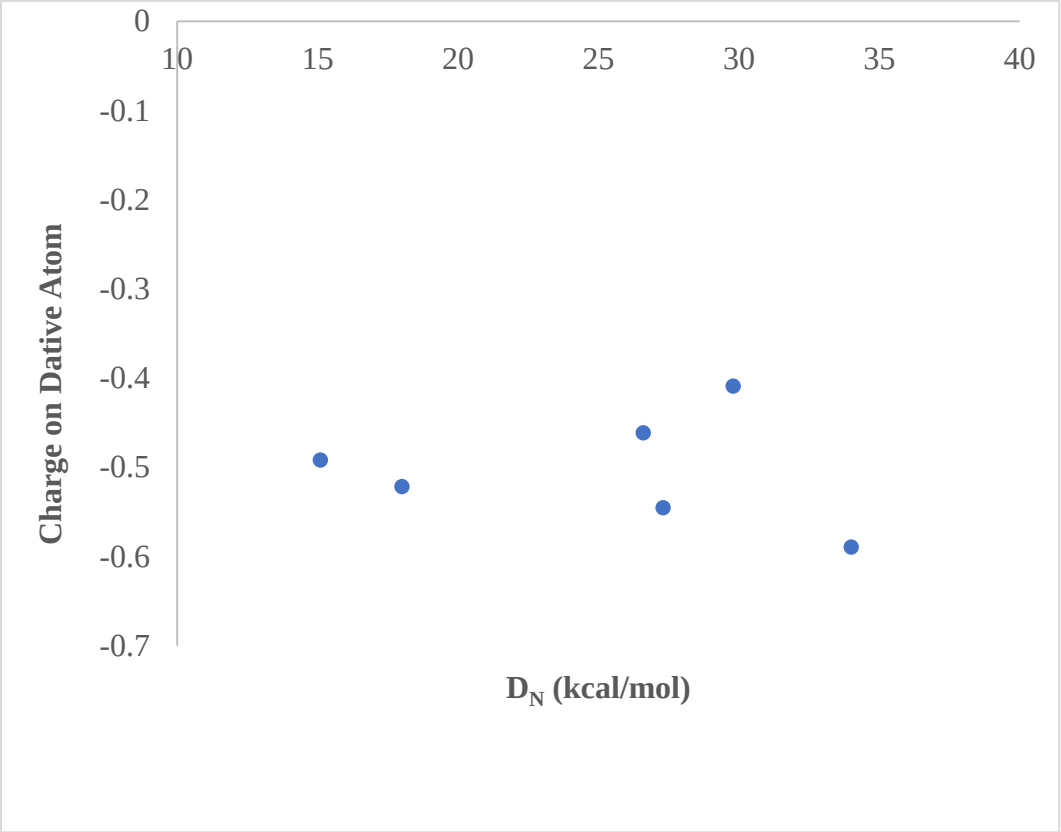

Figure 2.16: Correlation between the charge of the dative atom and the D_N.

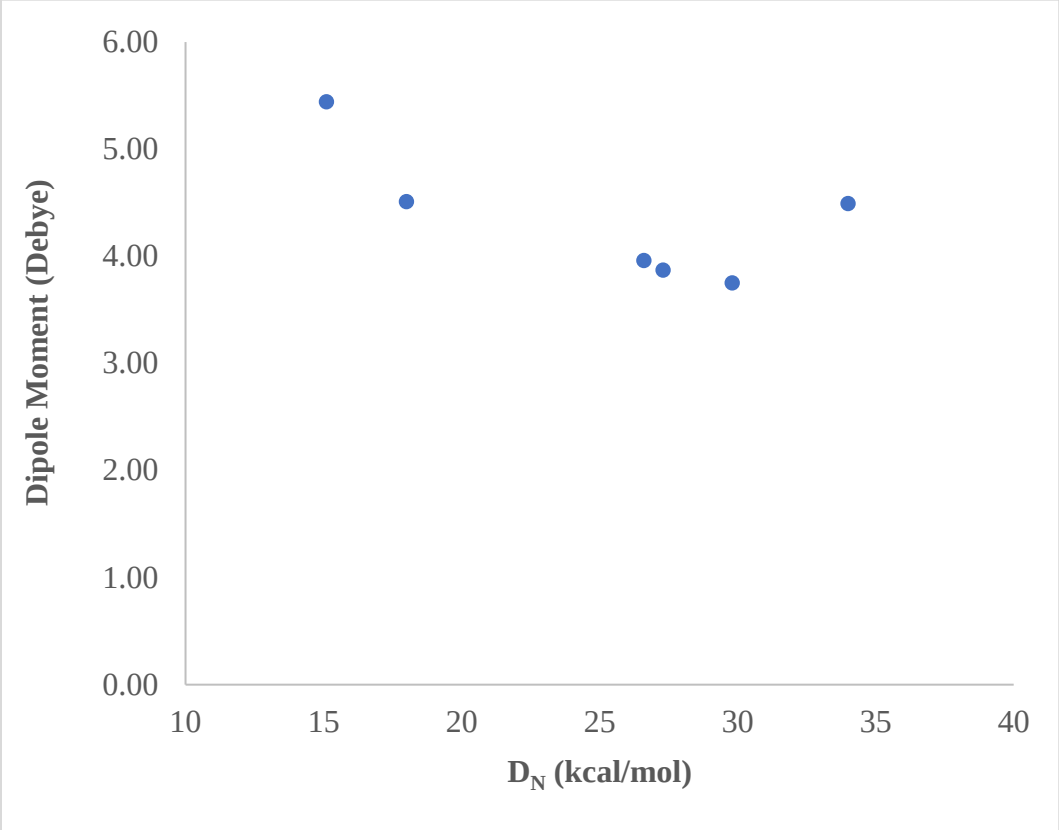

Figure 2.17: Correlation between the dipole moment of the solvent and D_N.

2.3.2.5 Summary of Metric Studies

Overall, solvents with higher Gutmann Donor Number (D_N) values have a stronger (more negative) binding energy, and a higher UMBO (and UMBO of the complex). And they generally exhibit shorter coordination distances of the solvent molecules to the Pb^{2+} center, and longer Pb–I bonds (leading to a more substantial reduction in Pb–I bond saturation) than solvents with lower D_N solvents. In contrast, they are not identifiable by their size (as described by the MVEE), atomic charge, or polarity. Of the metrics studied, the binding energy**,** length of the Pb–I bond, as well as the MBO of the Pb–I bond and the UMBO of the complex presented the strongest (and most distinguishable) correlation with the experimentally observed efficacy of the solvents in this study as denoted by the D_N.

This suggests that these metrics, along with the D_N, are useful for describing the efficacy of solvents in solubilizing the lead salt. Although the bond saturation properties (MBOs and UMBOs) are much easier to calculate, the binding energy provides the strongest correlation with the D_N. This study has revealed the governing features of solvents during their interaction with, and subsequent solubilization of, the solute studied here (PbI_2). For instance, it is possible that the delayed nucleation observed in high D_N solvents [55, 77] could be due to the extent to which they push halides away from the Pb^{2+} center (longer Pb–I bonds and weaker Pb–I bond saturation). Future studies could confirm or disprove this hypothesis. Summary Tables 2.2, 2.3, and 2.4, which depict all the properties determined in the study, are presented below.

Solvent	D_N (kcal/mol)	BE(Complex) kcal/mol	Charge on 'O'/'S'	Dipole Moment (Debye)
DMPU	34.0	–42	–0.59	4.49
DMSO	29.8	–37	–0.41	3.75
NMP	27.3	–32	–0.55	3.87
DMF	26.6	–32	–0.46	3.96
GBL	18.1	–25	–0.52	4.51
PC	15.1	–20	–0.49	5.44

Table 2.2: Summary of Binding Energy of solvents to PbI_2 (BE) and charge distribution results associated with six complexes between PbI_2 and 4 Solvent molecules, listed in order of increasing (less negative) Binding Energy. Rows are colored as in Table 2.1.

Solvent	DN (kcal/mol)	Bond of interest	MBO (Pb–O | Pb–I)		UMBO (Solvent | Complex)	
DMPU	34.0	C=O	0.19	0.40	0.18	0.46
DMSO	29.8	S=O	0.18	0.45	0.44	0.56
NMP	27.3	C=O	0.18	0.50	0.08	0.37
DMF	26.6	C=O	0.18	0.50	0.12	0.36
GBL	18.1	C=O	0.17	0.60	–0.04	0.22
PC	15.1	C=O	0.17	0.63	–0.05	0.21

Table 2.3: Summary of the results for the UMBOs (Original and Complex) and MBOs (Pb–I and Pb–O) associated with the six PbI_2–4Solvent complexes, listed in order of increasing Pb–I MBO. Rows are colored as in Table 2.1.

Solvent	DN (kcal/mol)	(MVEE) A^3	Pb–Solvent CD (Å)	Pb–Iodide CD (Å)	Pb–I Extension (%)
DMPU	34.0	77	2.65± 0.04	3.27± 0.01	12
DMSO	29.8	22	2.66 ± 0.1	3.21± 0.02	10
NMP	27.3	48	2.64 ± 0.1	3.23± 0.01	10
DMF	26.6	30	2.66 ± 0.1	3.20± 0.03	9
GBL	18.1	43	2.81 ± 0.2	3.07± 0.02	5
PC	15.1	43	2.85 ± 0.2	3.06± 0.02	5

Table 2.4: Summary of Pb–Solvent, Pb–I Coordination Distances (CD), Pb–I Extension (%), and MVEE results associated with the six PbI_2–Solvent systems, listed in order of increasing Pb–I extension. Rows are colored as in Table 2.1.

2.4 Computational Investigation of Sulfur–donor Solvents for MAPI Processing

In collaboration with J. Clay Hamill and Prof. Y.–L. Loo at Princeton, we set out to confirm the hypothesis that strongly coordinating solvents suppress the formation of homogeneous nuclei, and ultimately lead to an improved final film morphology [55, 77]. We studied this by comparing solvents containing sulfur as the donor atom, *i.e.,* 'S–' donor solvents, with 'O–' donor solvents, which have oxygen as the donor atom. Knowing that Pb–S bonds/interactions are stronger than Pb–O guided the hypothesis that Pb–S bonds formed from the coordination of 'S–'donor solvent molecules to PbI_2 would be stronger than Pb–O bonds formed from oxygen solvents coordinating with the Pb^{2+} center [118–120].

Further, based on HASB theory, 'S–' donor solvents are "softer" bases than 'O–' donor solvents and should form stronger complexes with PbI_2, a "softer" acid [109, 110]. To study these interactions computationally (and to complement the experimental procedure adopted to produce these films) – we studied three systems: (1) PbI_2 with solvent (mimicking dissolution of the lead salt), (2) PbI_2, MAI and solvent (the components of perovskite formation), and (3) PbI_2, MAI, and mixed solvents (containing both the 'S–' donor solvent and its oxygen counterpart). All simulations were performed using DFT.

Table 2.5 below highlights the size and charge of the dative atom and the dipole moment of the sulfur–donor solvents against their oxygen counterparts. 'S–' donor solvents are slightly larger in size than their 'O–' donor counterparts; they have a correspondingly lower charge density on the dative 'S' atom, and they have a larger dipole moment. Table 2.5 also shows that the UMBO of

‘S–’ donor solvents is greater than their ‘O–’ donor counterparts, hinting at a greater propensity for solubilization for ‘S–’ donor solvents.

Solvent	Molecular Structure	VMD Image	UMBO	(MVEE) A^3	Charge on 'O'/'S'	Dipole Moment (Debye) –
DMF		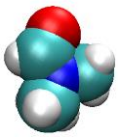	0.12	30	–0.46	3.96
DMTF	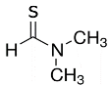	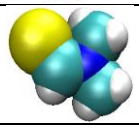	0.29	32	–0.29	4.83
NMP		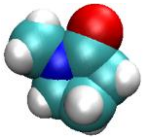	0.08	48	–0.55	3.87
NMPT		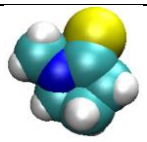	0.36	53	–0.37	4.83

Table 2.5: Comparison of properties between 'S–' donor and 'O–' donor solvents covered in this study. 'S–' donor solvents selected: Dimethylthioformamide (DMTF) and N–methylpyrrolidone thione (NMPT). 'O–' donor: N, N–dimethylformamide (DMF) and N–methyl–2–pyrrolidone (NMP). Color scheme for Visual Molecular Dynamics (VMD) images: Oxygen (●), Sulfur (●), Carbon (●), Hydrogen (●), Nitrogen (●)

2.4.1 System 1 – Dissolution of Salt

The Loo group conducted experiments in pure solvents (DMF, NMP, DMTF, NMPT) in PbI_2 in a 12:1 solvent: PbI_2 ratio. Experimental results for the CN are listed in Table 2.6 below. We ran DFT simulations of the experimentally observed complexes (*via* the CN) for the four solvent–PbI_2 systems to reveal information about the binding strength (represented by the binding energy – see Equation 2.3) of the 'S–' donor solvents relative to their 'O–' donor counterparts. The UMBO of the formed complex was also calculated to complement our binding propensity results, as shown in Table 2.7. Pb–Solvent and Pb–I bond distances from our DFT runs were calculated and compared with the experimentally determined bond distances, see Table 2.8.

Our simulation was set up with four 'O–' or 'S–' donor solvents coordinating to the Pb^{2+} center in order to replicate the average coordination observed experimentally by EXAFS data from the Loo group – see Tables 2.6 and 2.7 – and allowed to relax using a DFT simulation employing a B97–D3 functional. The binding energy of four solvent molecules to PbI_2 (BE) and the UMBO for the complex indicate that the strength of the complex formed *via* 'S–' donor coordination is greater than the complex formed *via* 'O–' donor coordination. Experimental coordination distances also agree with simulation results – see Table 2.5. Comparing oxygen–containing solvents with their 'S–' donor solvent analog (DMF to DMTF, and NMP to NMPT), we found that sulfur–containing solvents approach less closely to the Pb^{2+} center than their oxygen–containing counterparts. For example, the coordination distance for NMP was 2.6 ± 0.1 Å, but a larger distance, 3.1 ± 0.1 Å was observed for NMPT. Likewise, the value for DMF, 2.6 ± 0.1 Å, was lower than that for DMTF, 3.1 ± 0.1 Å. However, most of this 0.5 Å difference is accounted by the larger van der Waals radius of the sulfur atom (0.3 Å) [119, 121]. Thus, this observation

does not suggest that ‘S–’ donor solvents coordinate less strongly than their oxygen–counterparts as this distance does not influence the enthalpic differences between the formed clusters.

Sample	Shell	CN	Total CN
DMF	**Pb–O**	4.0 ± 0.5	6.0 ± 1.4
	Pb–S	N/A ± N/A	
	Pb–I (1)	1.3 ± 0.5	
	Pb–I (2)	0.7 ± 0.5	
DMTF	**Pb–O**	N/A ± N/A	6.2 ± 2.2
	Pb–S	4.2 ± 0.6	
	Pb–I (1)	1.6 ± 0.8	
	Pb–I (2)	0.4 ± 0.8	
NMP	**Pb–O**	4.0 ± 0.3	5.7 ± 0.5
	Pb–S	N/A ± N/A	
	Pb–I (1)	1.0 ± 0.1	
	Pb–I (2)	0.8 ± 0.1	
NMPT	**Pb–O**	N/A ± N/A	5.5 ± 1.3
	Pb–S	3.9 ± 0.5	
	Pb–I (1)	0.7 ± 0.2	
	Pb–I (2)	0.9 ± 0.6	

Table 2.6: System (1). Coordination Number, CN, of two pairs of ‘S–‘ donor and ‘O–‘ donor solvents (NMPT/NMP and DMTF/DMF) and iodide anions to a Pb^{2+} center in a pure solvent and PbI_2 system – no MAI is present.

Solvent	Complex (PbI_2 with four Solvents)	BE (kcal/mol)	UMBO for the complex
DMF	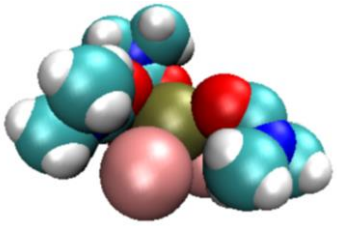	–32	0.39
DMTF	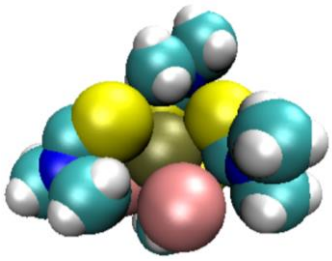	–38	0.47
NMP	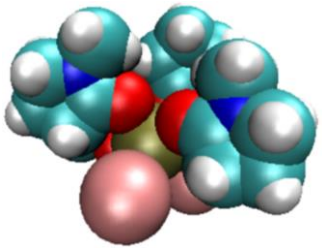	–32	0.39
NMPT	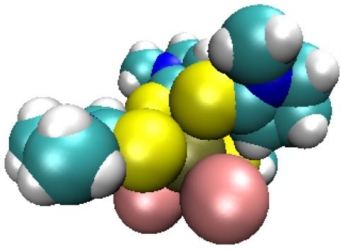	–45	0.48

Table 2.7: Key characteristics of the PbI_2–Solvent complex observed experimentally by the Loo group (namely, four solvent molecules of DMF and two iodide anions coordinating with Pb^{2+}). This Table shows two metrics of complex strength: the binding energy of four solvent molecules to PbI_2 (BE) and the UMBO for the complex. Color key as in Table 2.5.

Solvent	Pb–Solvent bond distance (Å) (DFT)	Pb–Solvent bond distance (Å) (EXAFS)	Pb–I bond distance (Å) (DFT)	Pb–I bond distance (Å) (EXAFS)
DMF	2.66 ± 0.04	2.62 ± 0.11	3.20 ± 0.03	3.20 ± 0.10
DMTF	3.13 ± 0.02	2.97 ± 0.12	3.20 ± 0.03	3.28 ± 0.15
NMP	2.64 ± 0.04	2.56 ± 0.14	3.23 ± 0.01	3.20 ± 0.07
NMPT	3.14 ± 0.02	3.04 ± 0.12	3.21 ± 0.02	3.23 ± 0.08

Table 2.8: Pb–I and Pb–Solvent bond distances for the four PbI_2–Solvent complexes calculated from DFT simulations and compared to EXAFS unpublished results reported by the Loo group.

2.4.2 System 2 – Perovskite Formation

The Loo group has also conducted experiments with PbI_2 *and* MAI in *pure* solvents (DMF, NMP, DMTF, NMPT) in a ratio of 1:1:12 (PbI_2: MAI: Solvent). This is noteworthy as a study intended to uncover the fundamentals of perovskite thin film formation since most studies look only at solvent blends. Experimental results for the coordination number are listed in Table 2.9 below. And, as in system 1, we calculated the binding energy, UMBO, and bond distances of the formed complexes – see Table 2.10 and 2.11.

EXAFS data was unable to report the presence the MA molecule in solution, so DFT was consulted to confirm the favourability of MA complexation to the experimentally observed PbI_5 complex. MA was included because it stabilized the complex – DFT results suggests that the complexation of MA to the PbI_5 complex was 14 kcal/mol more stable than the scenario in which no MA was included in the complex. As a result, the simulation of the complex was set up with a single oxygen– or sulphur– donor solvent molecule coordinating to the Pb^{2+} center and allowed to relax using DFT and the same procedure to dissolve the lead salt. This emulates the experimental situation in which, the inclusion of MA forms a PbI_5MA complex in solution. As for the case of the pure solvent coordinating to PbI_2 (in the absence of MAI; *i.e.*, system (1)), we found that the experimentally determined coordination distances agree with those obtained from simulation. Further, the binding energy and UMBO results reflect the improved efficacy of 'S–' donor solvents relative to 'O–' donor solvents.

Sample	Shell	CN	Total CN
DMF	**Pb–O**	1.4 ± 0.2	6.1 ± 0.9
	Pb–S	N/A ± N/A	
	Pb–I (1)	2.0 ± 0.3	
	Pb–I (2)	2.7 ± 0.4	
DMTF	**Pb–O**	N/A ± N/A	6.5 ± 1.0
	Pb–S	1.3 ± 0.2	
	Pb–I (1)	1.8 ± 0.3	
	Pb–I (2)	3.5 ± 0.5	
NMP	**Pb–O**	0.8 ± 0.5	5.8 ± 1.1
	Pb–S	N/A ± N/A	
	Pb–I (1)	2.5 ± 0.2	
	Pb–I (2)	2.5 ± 0.4	
NMPT	**Pb–O**	N/A ± N/A	6.2 ± 0.7
	Pb–S	1.2 ± 0.1	
	Pb–I (1)	2.5 ± 0.2	
	Pb–I (2)	2.4 ± 0.4	

Table 2.9: System (2). Coordination Number, CN, of solvents and iodide anions to a Pb^{2+} center in a pure solvent, PbI_2 system with MAI present. Results are presented for two pairs of 'O–' and 'S–' donor systems (NMPT/NMP and DMTF/DMF).

Solvent	Complex ($PbMAI_5$ with one Solvent)	BE (kcal/mol)	UMBO for the complex
DMF	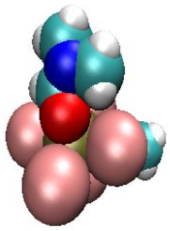	–9	0.40
DMTF	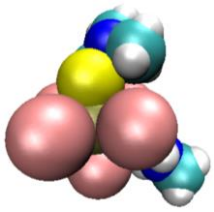	–12	0.48
NMP	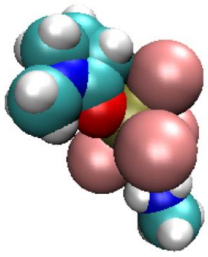	–10	0.41
NMPT	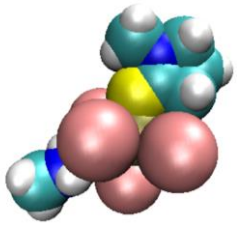	–20	0.54

Table 2.10: Key characteristics of the PbI_2–MAI–Solvent complex observed experimentally by the Loo group (consisting of one solvent molecule of DMF and five iodide anions coordinating with Pb^{2+}). This Table shows two metrics of complex strength: the binding energy of one solvent molecule to PbI_5MA (BE) and the UMBO for the complex. Color key as in Table 2.5.

Solvent	Pb–Solvent bond distance (Å) (DFT)	Pb–Solvent bond distance (Å) (EXAFS)	Pb–I bond distance (Å) (DFT)	Pb–I bond distance (Å) (EXAFS)
DMF	2.56 ± 0.01	2.57 ± 0.14	3.29 ± 0.0	3.22 ± 0.11
DMTF	2.98 ± 0.03	2.98 ± 0.08	3.30 ± 0.01	3.23 ± 0.09
NMP	2.57 ± 0.02	2.56 ± 0.13	3.29 ± 0.01	3.30 ± 0.13
NMPT	3.03 ± 0.0	2.98 ± 0.09	3.29 ± 0.0	3.30 ± 0.13

Table 2.11: Comparisons of Pb–I and Pb–Solvent bond distances for the four PbI_2–MAI–Solvent complexes calculated from both DFT simulations and EXAFS results reported by the Loo group.

2.4.3 System 3 – Solvent Mixture

Lastly, experiments were conducted with PbI_2 and MAI in a mixture containing both 'O–' and 'S–' donor solvent molecules. 'O–' donor solvents (DMF and NMP) were mixed with their 'S–' donor counterparts with different ratios. Figures 2.18 and 2.19 highlight the change in coordination number of the solvent to the Pb^{2+} center observed at different ratios of 'O–' and 'S–' donor solvents. To study the competition between 'O–' and 'S–' donor solvents for the Pb^{2+} center, we compared the energy associated with 'S–' donor solvent coordination to that associated with only 'O–' donor solvent coordination at a 1:1 ratio of the 'O–' donor and its 'S–' donor counterpart (DMF:DMTF and NMP:NMPT).

This method involved fixing 'O–' or 'S–' donor solvent coordination to PbI_5MA and packing these solvents in a separate box. All the species in the box were optimized using a B97–D3 functional in DFT. The first simulation box contained a PbI_5MA–Solvent complex (with the solvent being an 'O–' donor), simulated with a system containing one less 'O–' donor solvent molecule than the 'S–' donor solvents. These systems were then modified by switching all the 'O–' donor solvents in boxes 1 and 2 with 'S–'donor solvents, changing the coordination to the Pb^{2+} center in PbI_5MA from an 'O–' to a 'S–' donor and the composition of 'S–' and 'O–' donor solvents; see Figure 2.20. An energetic comparison of these two boxes was made to reveal which was the enthalpically favoured configuration, *i.e.*, whether 'S'–donor solvent coordination is more favoured than 'O–' donor solvent coordination in a mixed solvent system, factoring into account how the 'S–' donor solvents interact with their oxygen counterparts.

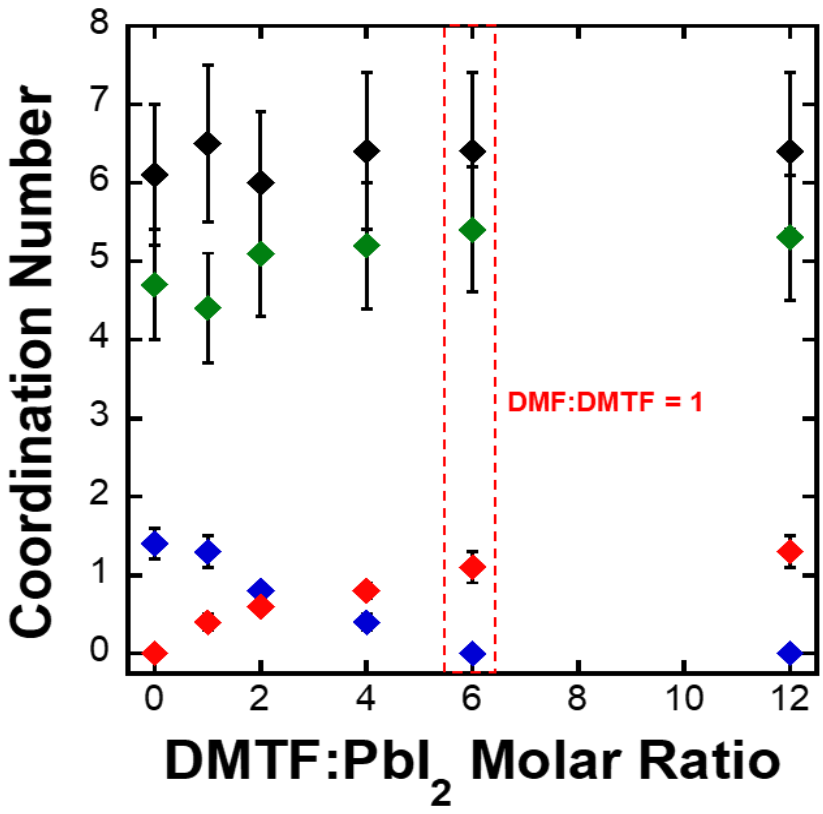

Figure 2.18: Currently unpublished experimental data from the Loo group showing the coordination number of each species to Pb^{2+} as a function of the DMTF: PbI_2 molar ratio in solution. As the DMTF: PbI_2 ratio increases, Pb–O coordination (♦) decreases while Pb–S coordination increases (♦). Iodide coordination (♦) and total coordination (♦) remain constant. When DMF and DMTF are equimolar in the solution (indicated by the red rectangle), only Pb–S and Pb–I coordination is observed.

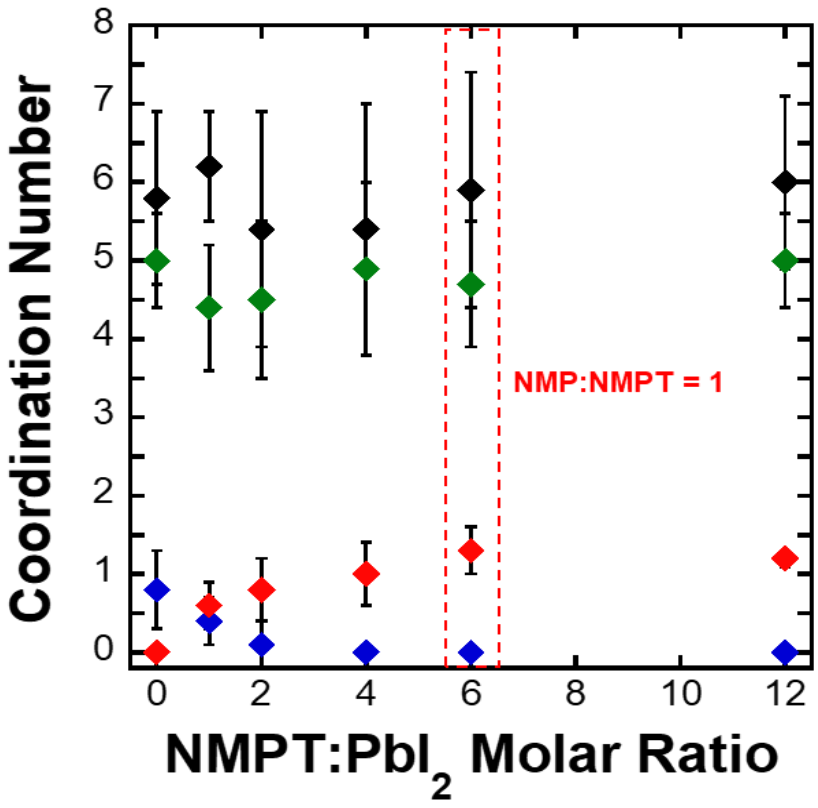

Figure 2.19: Results as in Figure 2.18 but substituting NMPT for DMTF. Currently unpublished experimental data from the Loo group showing coordination number of each species to Pb^{2+} as a function of the NMPT: PbI_2 molar ratio in solution. Similar results are found to those in Figure 2.18.

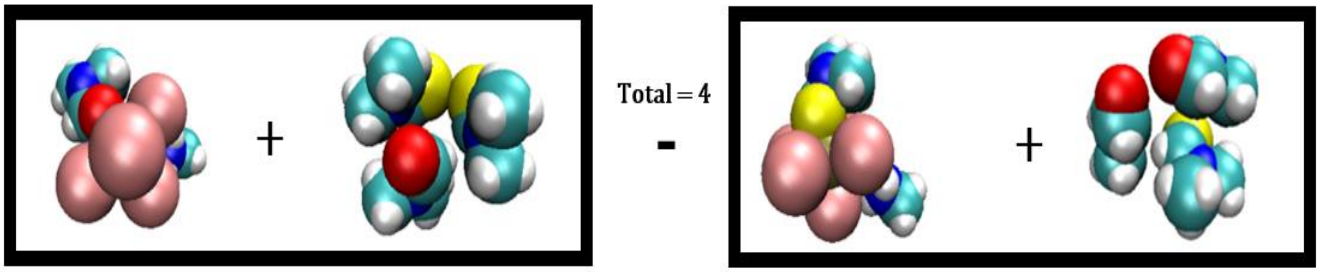

Figure 2.20: Computational approach used to determine preferential solvent coordination in a mixed solvent system containing 'O–' and 'S–' donor molecules. The DFT energy of the first box ('O–' donor coordination) is compared to the energy of the second box ('S–' donor coordination). Color scheme as in Table 2.5.

Our DFT results revealed that sulfur coordination to the Pb^{2+} center is energetically preferred over oxygen coordination in both the systems we studied (NMPT/NMP and DMTF/DMF) given equal ratios of 'S–' donor and 'O–' donor solvents. The results were compared for a 1:1 ratio but considering an increasing number of solvents in the system (starting at '1:1' molecule and ending at a ratio of '6:6'solvent molecules). These results also stipulate that the difference in interaction between 'O–' and 'S–' to the Pb^{2+} center is more pronounced in NMPT/NMP, which have ring structures, than that of DMTF and DMF – see Table 2.12. This also agrees with the experimental observation by the Loo group that lower amounts of NMPT (1:11 NMPT to NMP ratio) are needed to cause a change in coordination from 'O–' to 'S–' in an NMPT: NMP mixture. However, a 4:8 DMTF to DMF ratio, which has a greater 'S–' donor concentration, is required for change in Pb^{2+} coordination from 'O–' to 'S–' donor in a DMTF: DMF solvent mixture. Also note that the computational results presented here are enthalpic energy values (at 0 K) and do not correspond to free energy values; these simulations do not consider entropic preferences for each complex formed. However, these results do suggest that the coordination of solvents to salts in this scenario is primarily dictated by atom–atom 'enthalpic' interactions between the 'O–' (or 'S–') atom and the Pb^{2+}, rather than by entropic considerations or guided by kinetics.

These results also point to the potential efficacy of NMPT as a solvent in processing the perovskite $PbMAI_3$: the binding energy and UMBO metrics for NMPT place it at competitive levels with strong solvents like DMPU and DMSO; see Tables 2.3 and 2.7. To confirm this, films were prepared by the Loo group with an 'S–' donor and 'O–' donor solvent mixture of DMF–NMPT, with DMF used as the bath solvent and NMPT as a solvent additive. As seen in Figure 2.21, as the NMPT fraction increases, the morphology and coverage of the films is improved. When the

ratio of NMPT:DMF is at 0.5:1, the film exhibits full coverage and a grain–like morphology similar to that obtained for high–efficiency HOIP devices [122].

N	ΔE (DMTF–DMF)	ΔE (NMPT–NMP)
1	–4	–11
2	–2	–10
3	–1	–11
4	–1	–8
5	–3	–12
6	–5	–15
AVG	–3 ±1	–12 ±2

Table 2.12: Energy differences between 'S–' donor solvent coordination and 'O–' donor solvent coordination for NMPT–NMP and DMTF–DMF pairs at equal solvent ratios (1:1) but varying the total number of solvent molecules (N) in the simulation. Results show that *ab initio* results indicated that 'S–' donor coordination in the NMPT/NMP mixture (at an equal solvent ratio) was substantially (12 kcal/mol) more stable than 'O–' donor coordination, whereas for the DMTF/DMF mixture this gap was only 3 kcal/mol.

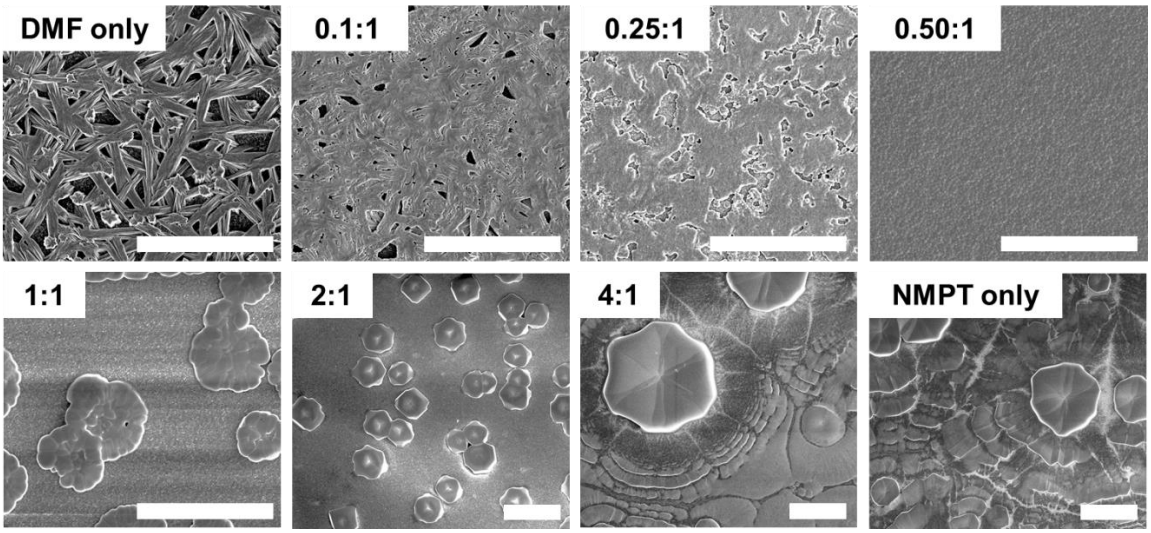

Figure 2.21: Unpublished data from the Loo group at Princeton presented with their permission showing experimental SEM images of $MAPbI_3$ thin films processed from precursor solutions comprising 1:1 MAI: PbI_2 to which NMPT was added in increasing concentrations to a DMF and Salt solution. No antisolvent treatment was applied to the films. Scale bar: 20 μm.

2.5 Iodoplumbate Formation in Perovskite Films in Solution

Having studied the strength of different solvent–PbI_2 complexes, we turn our attention to predicting the type of species we could potentially observe in these different solvent environments. We have studied and compared the formation of a series of Pb–based iodoplumbate complexes (PbI_3^- – PbI_5^{3-}) to [PbI_2 – solvent]. Iodoplumbates are perovskite progenitor complexes that are often implicated at the beginning of the nucleation process that produces perovskite crystals in solution; iodide coordination to Pb^{2+} center increases to form smaller nuclei that induce the growth of the perovskite film [123, 124]. Iodoplumbates also form *via* the presence of excess iodide ions in the solution mixture [120, 121, 125, 126].

This work intends to highlight the preferential coordination and complex formation of strong solvents (like 'S–' donor solvents, especially DMPU), as well as the lower coordination of "poor" solvents (*e.g.*, PC and GBL), to iodide ions originating from organic salts (MAI) and system additives (HI, NH_4I) [123]. All simulation results were derived from the DFT code within ORCA using the B97–D3 functional and the accurate triple–zeta basis set, def2–TZVP. Iodide species were represented by the iodide ion (their cations dissociate in the medium to form iodide anions with no difference between potassium (K) or MA) [127, 128]. Alternative pathways exist that could promote the formation of these species and precursors (iodoplumbates and solvated complexes) in solution. Figure 2.22 highlights the different coordination approaches that the inorganic salt, PbI_2, could adopt during the formation of either perovskite precursors.

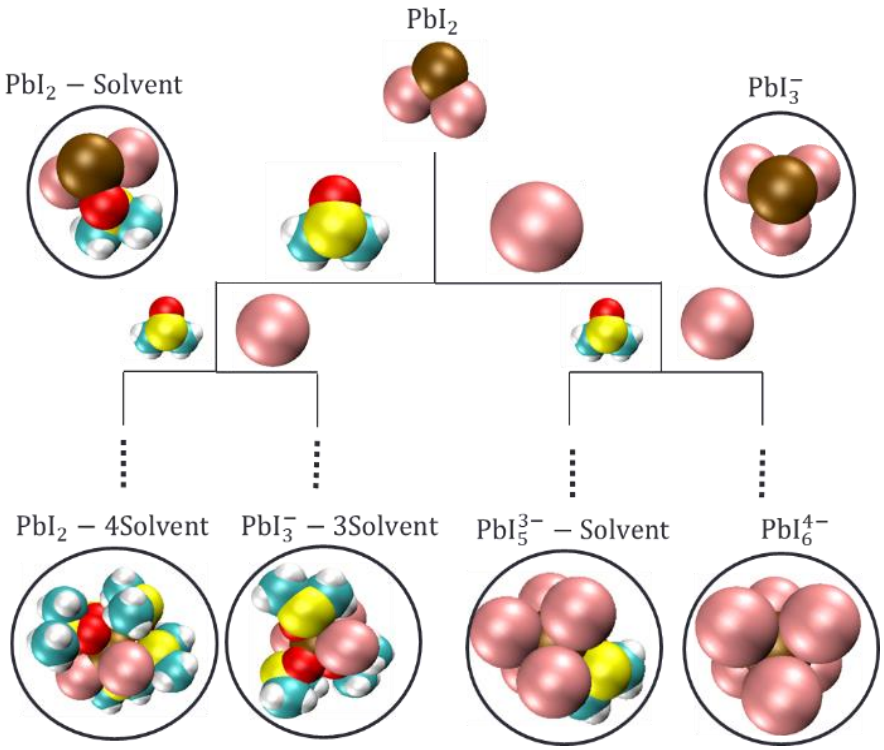

Figure 2.6: Illustration of the different formation pathways for iodoplumbate formation in a solvent environment (S) from PbI_2. Color scheme for Visual Molecular Dynamics (VMD) images: Oxygen (●), Sulfur (●), Carbon (●), Hydrogen (●), Lead (●), Iodide (●).

We have studied the enthalpic preference of iodoplumbate complexes in DFT–generated complexes [PbI_2, PbI_3^-, PbI_4^{2-}, PbI_5^{3-}, and PbI_6^{4-}]; see Figure 2.23. These results provide insight into the most enthalpically preferred iodoplumbate complexes for each of the solvents in this study. We hypothesize that higher–order iodoplumbates [PbI_5^{3-} and PbI_6^{4-}] are more enthalpically favourable in weakly coordinating solvent environments, leading to more rapid nucleation in these solutions [55, 129]. Rapid nucleation of these species has been linked to unfavourable morphologies (smaller grains and more grain boundaries) [55, 129]. By fixing the Pb^{2+} coordination number at 6, with coordination arising from bonding with iodides and solvent molecules, we have grouped the preferred iodoplumbate complex formation as: **Lower Order** (the solvent environment supports the formation of PbI_2 and PbI_3^-), **Unclear** (the solvent environment supports the formation of either complex, indicated by a very similar BE between them), **Higher Order** (the solvent environment supports the formation of PbI_4^{2-}, PbI_5^{3-}, and PbI_6^{4-}). The following subsections highlight the determination of this preference in 16 different solvent environments and whether experimental metrics like Gutmann's donor number (D_N) can adequately predict the occurrence of these precursors in solution.

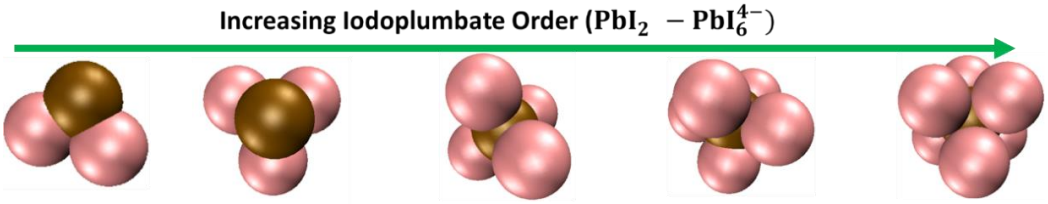

Figure 2.7: The five iodoplumbate complexes studied here (PbI_2 to PbI_6^{4-}). Color scheme as in Figure 2.22.

2.5.1 Predicting the Formation of Iodoplumbate Complexes in Solution

We have studied the usefulness of the D_N to predict the strength of PbI_2 – solvent complexes. As previously described, the D_N is an experimental metric that measures the Lewis basicity of a solvent as the enthalpy of solvation from its coordination with antimony pentachloride ($SbCl_5$) in dilute solution of 1,2 dichloroethane [110].

We have modelled the antimony–containing system used in the experimental determination of the D_N using DFT by representing the coordinating solvent as an explicit single solvent molecule coordinating to an Sb^{5+} center, with 1,2 dichloroethane as an implicit solvent with a dielectric constant value of 10.4, and $SbCl_5$ modeled as an explicit molecule. The experimental determination of the D_N is based on the pictorial representation and the equations shown in Figure 2.3. To complement the Loo group's experimental model, we have also provided a VMD image and the binding energy of solvent to $SbCl_5$ as determined from the equations:

$$SbCl_5 + Solv \rightarrow SbCl_5 - Solv \tag{2.4}$$

$$\Delta E_{binding} = E[SbCl_5 – Solv] – E[SbCl_5] – E[Solv] \tag{2.5}$$

We have used the binding energy as a metric to represent the D_N of fourteen solvents – a molecular representation of this calculation is shown in Figure 2.24. We then plotted the correlation of these results with the solvent's respective D_N value; see Figure 2.25. We also investigated the binding energy of solvents to PbI_2 (which occurs experimentally during the dissolution of PbI_2). This system was previously outlined in Equation 2.3 and Figure 2.5.

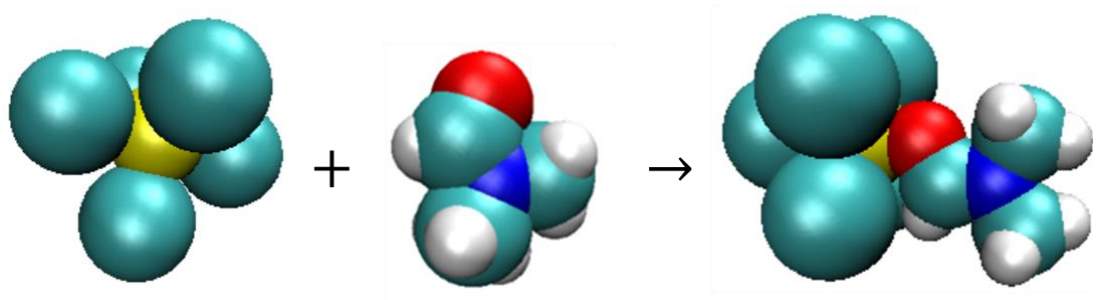

Figure 2.8: Molecular representation of $SbCl_5$–Solvent complex formation from Figure 2.3. Color scheme for Visual Molecular Dynamics (VMD) images: Oxygen (●), Antimony (●), Carbon (●), Hydrogen (●), Nitrogen (●), Lead (●), Iodide (●).

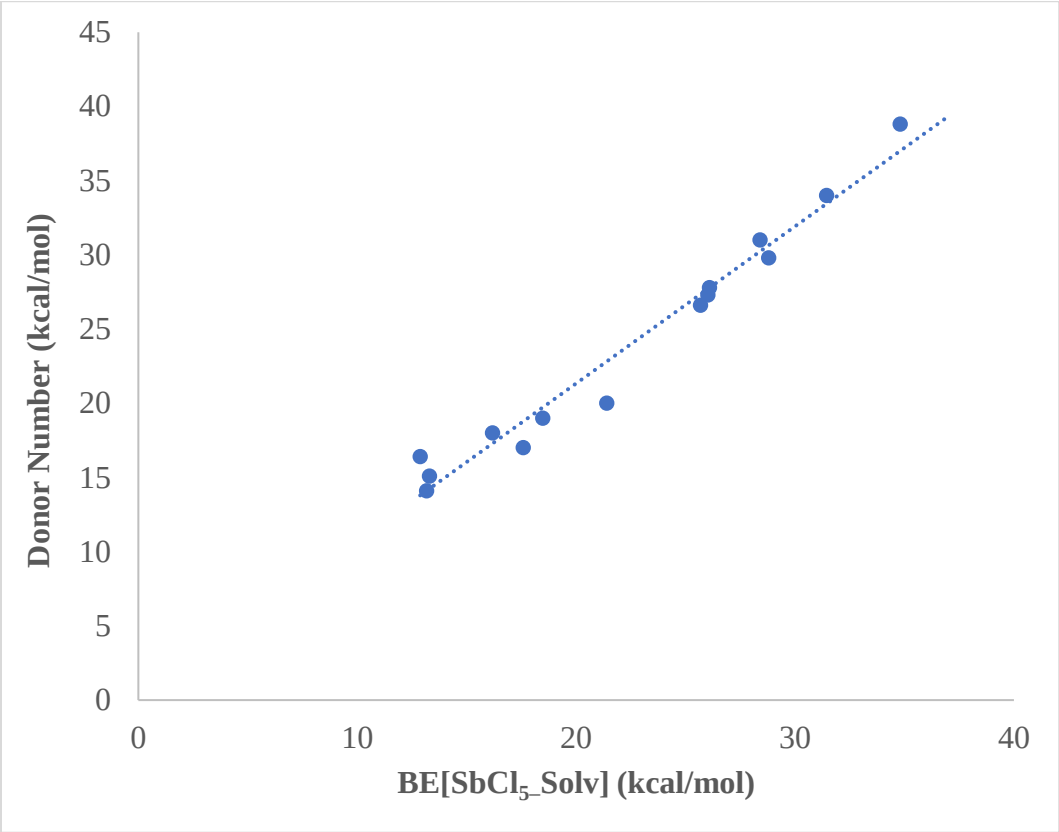

Figure 2.25: Binding energy of a single solvent molecule to $SbCl_5$ and its correlation with the D_N, showing a strong linear trend, with an $R^2 = 0.97$.

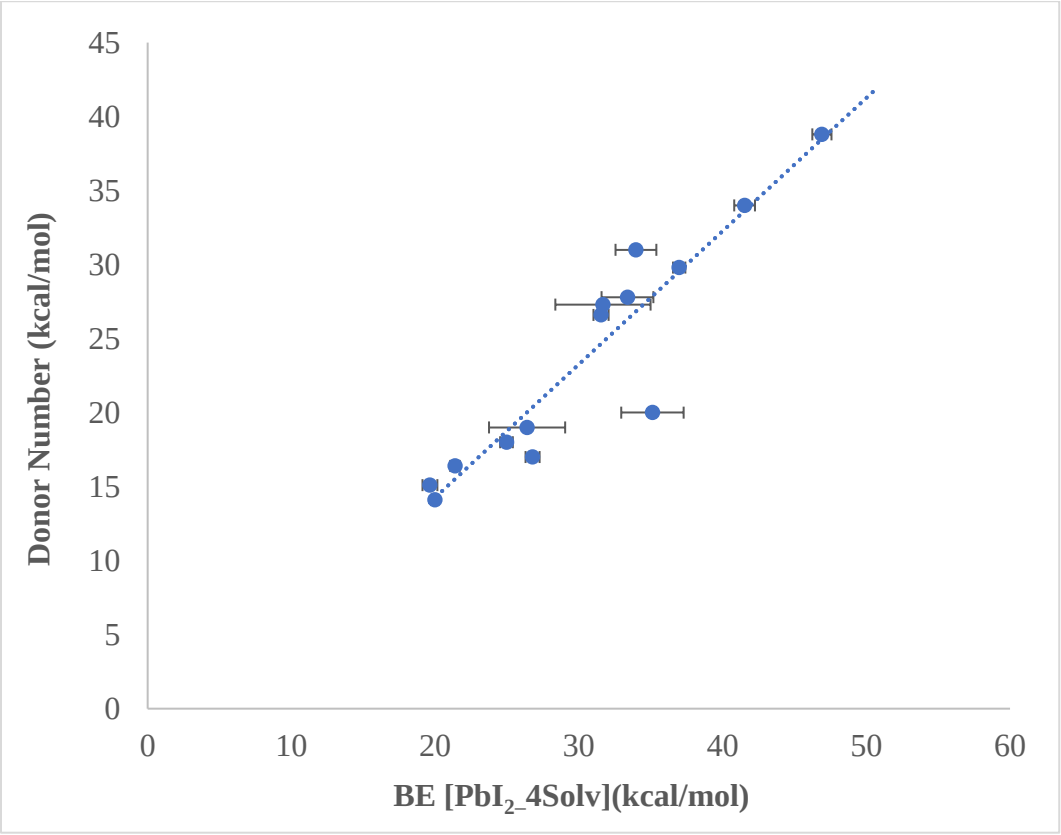

Figure 2.26: Binding energy of four solvent molecules to PbI_2 and its correlation with the D_N showing a much weaker linear trend, with an $R^2 = 0.87$. Error bars are obtained from the lowest four energies from a set of eleven DFT simulation runs.

Although antimony (Sb) and lead (Pb) are transition metal atoms, there is a difference in the most preferred oxidation states of these two atoms; Sb has an oxidation state of +5, while Pb prefers an oxidation state of +2 [110, 117, 131]. The resulting plot indicates that the binding energy of a solvent molecule to $SbCl_5$ is very effective at predicting the D_N of the solvent (Figure 2.25; R^2 = 0.97) – the system it was designed for – but not for PbI_2 solvation (Figure 2.26; R^2 = 0.87). That is, the D_N does not describe the solvation of the lead salt as well as the other case, although it is unclear whether this extent of correlation is good enough. The binding energy also does not indicate whether a solvent is strong enough to coordinate over the iodide halides in the same solution. However, we can now estimate the D_N values of 'S–' donor solvents (NMPT and DMTF), together with the experimentally effective additive, THTO, whose D_N values were previously unreported. Based on the linear correlation presented in Figure 2.25, the estimated Gutmann donor number values for NMPT and DMTF were 33 kcal/mol and 32 kcal/mol for THTO. All three solvents are thus predicted to have very similar D_N values.

2.5.2 Relative Energy Metric (REM)

As an alternative to the D_N for describing solvent efficacy in lead–halide perovskite formation, we have developed a new method of predicting solvent efficacy in terms of the ability to dissolve lead salts (whether the solvent fully complexes with the Pb^{2+} center, or whether iodide coordination dominates, forming iodoplumbate complexes). The new metric we have proposed is designed such that a REM value greater than zero predicts the favourable complexation of solvents over halides to the Pb^{2+} center in solution. A value for the metric between –2 to 2 specifies no clear preference for lower– or higher– order iodoplumbates. Below zero would

indicate that solvents are enthalpically outcompeted by iodides in solution leading to the formation of higher–order iodoplumbate complexes (PbI_4 – PbI_6). Values of the metric above zero would indicate that these solvents have a greater tendency to coordinate with the Pb^{2+} center over the iodide anion, leading to the formation of lower–order iodoplumbate complexes (PbI_2 and PbI_3^-).

We call this metric the Relative Energy Metric (REM). It compares the energies of full solvent coordination to the Pb^{2+} center and non–coordinated iodide ions in a dielectric medium to a system in which only iodide anions coordinate to PbI_2 (forming PbI_6) with no solvent coordination to the Pb^{2+} center; see Equation 2.6. Both simulations were run in an implicit solvent medium represented as the dielectric of the solvent of interest. This additional simulation feature is the conductor–like polarizable continuum model (CPCM), an implicit solvation model, which approximates the solvents by a dielectric continuum, surrounding the solute molecules outside of a molecular cavity [131]. This metric can also be used to evaluate the preference for a single solvent complexing with a single halide by averaging the REM values (denoted below as 'AVG REM') over the number of solvents/halides, currently set at four; see Equation 2.7. This allows us to describe the enthalpic competition between solvent and halides for complexation with Pb^{2+}. Figure 2.27 depicts the molecular species involved in the determination of REM. Table 2.12 below ranks solvents based on their REM and AVG REM values:

$$\Delta E_{REM} = \text{System 1 } (E[PbI_2\text{–}4Solv]+E[4I^-]) - \text{System 2 } (E[PbI_6^{4-}] + E[4Solv]) \quad (2.6)$$

$$AVG(\Delta E_{REM}) = \frac{\text{System 1 } (E[PbI_2\text{–}4Solv]+E[4I^-]) - \text{System 2 } (E[PbI_6^{4-}] + E[4Solv])}{4} \quad (2.7)$$

In Equations 2.6 and 2.7, $E[PbI_2 – 4Solv]$ represents the energy from a PbI_2 salt complexed to four solvent molecules, $E[4I^-]$ is the energy of four iodide anions, $E[PbI_6^{4-}]$ is the energy contribution

from a full PbI_6 complex and, lastly, E[4Solv] is the energy corresponding to four solvent molecules. Equation 2.6 maintains both a charge and an atomic balance.

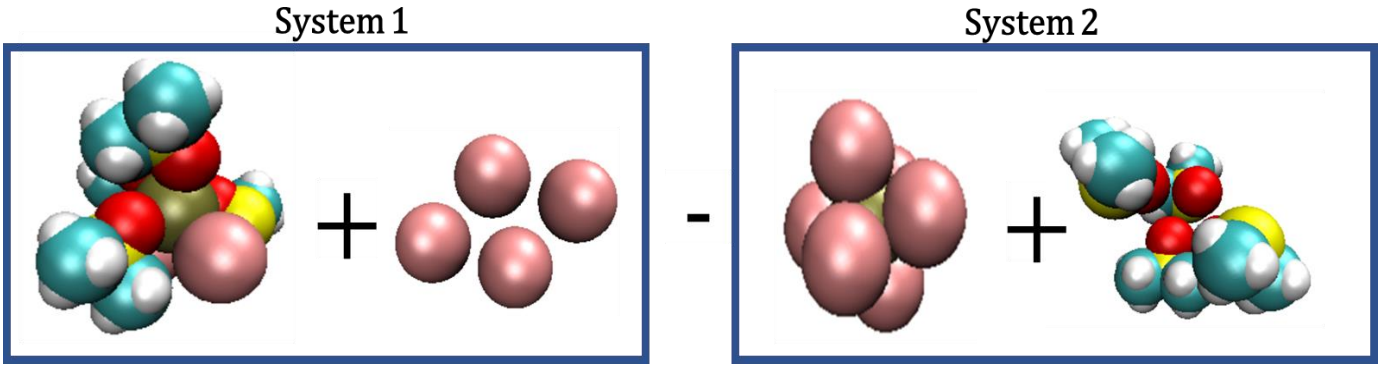

Figure 2.27: Molecular representation of a Relative Energy Metric (REM) calculation from Equation 2.6. Color scheme as in Figure 2.22.

IODOPLUMBATE ORDER	SOLVENT	REM	AVG REM
Lower Order (Strong Solvent)	HMPA	15	4
	NMPT	10	3
	DMPU	10	3
	THTO	7	2
	DMTF	6	1
	DMSO	5	1
Unclear (Moderate Solvent)	DEF	2	0
	DMAC	1	0
	DMF	0	0
	NMP	0	0
Higher Order (Poor Solvent)	ACETONE	–4	–1
	ETHANOL	–6	–1
	GBL	–8	–2
	EC	–12	–3
	PC	–13	–3
	ACN	–13	–3

Table 2.2: REM values for 16 different solvent molecules (ranked from highest to lowest REM), with popular solvents in perovskite processing identified using a **blue font.**

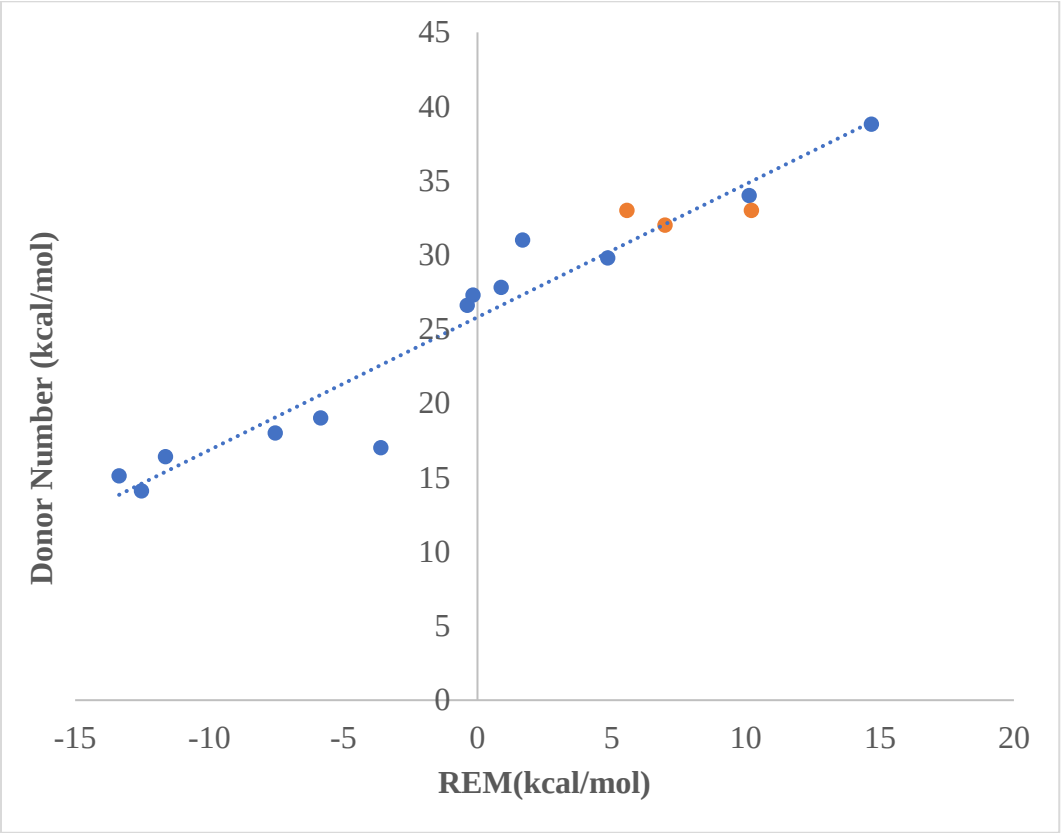

Figure 2.28: Correlation between the D_N and the REM metric for 13 out of 16 solvents (●). The remaining three solvents use computationally determined values for the D_N, namely the two 'S–'donor solvents and THTO, shown as (●), as no experimental D_N are available for these solvents. $R^2 = 0.93$.

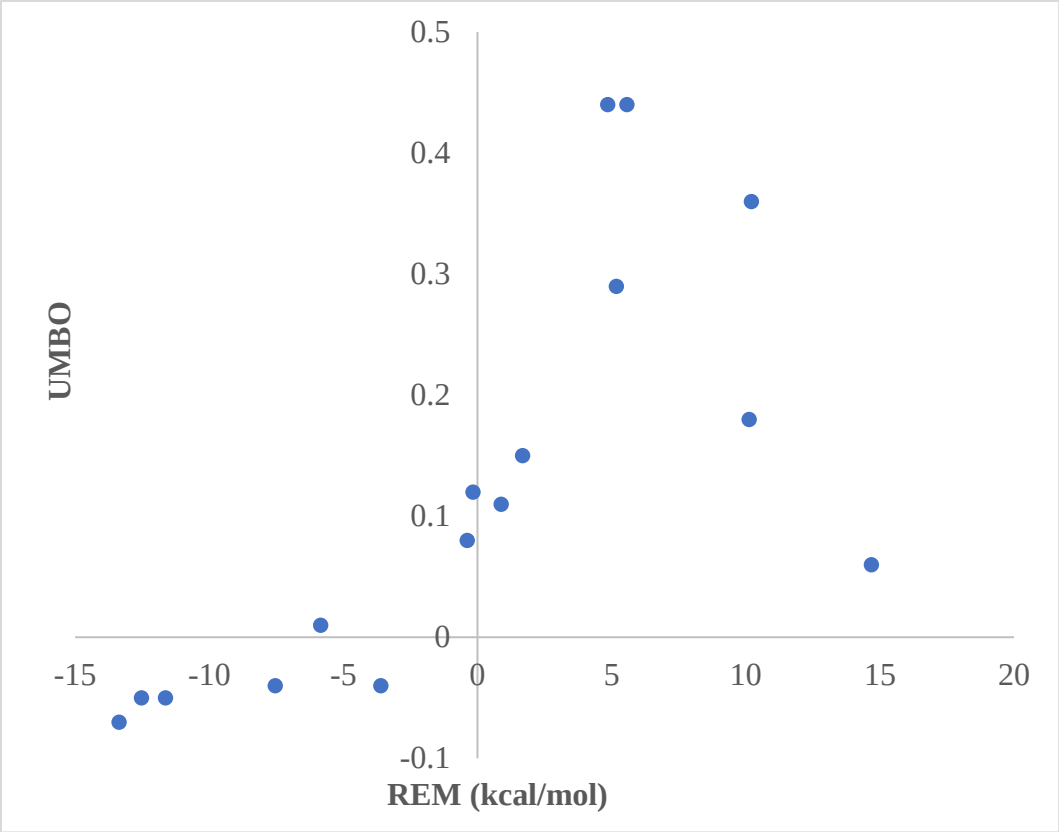

Figure 2.29: Correlation between the UMBO and REM metric for 16 solvents. Note the poor correlation between the variables, especially for positive values of REM.

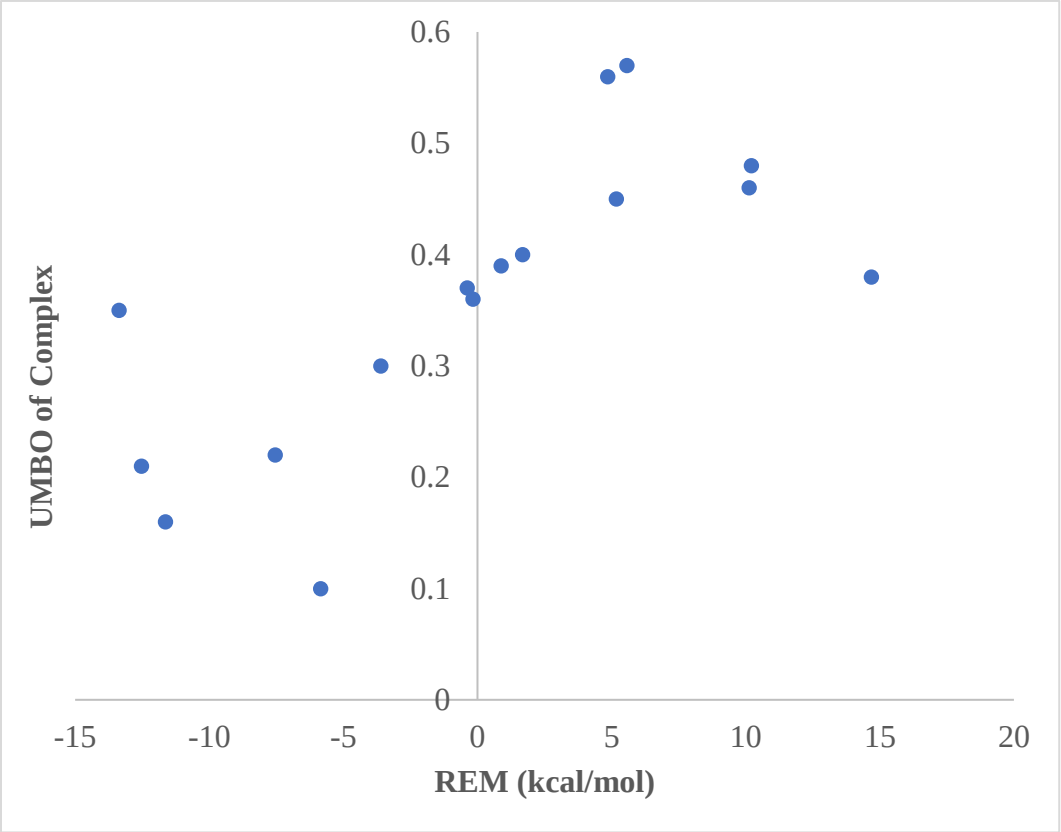

Figure 2.9: Correlation between the UMBO of the complex and the REM metric for 16 solvents. As in Figure 2.29, the correlation is poor.

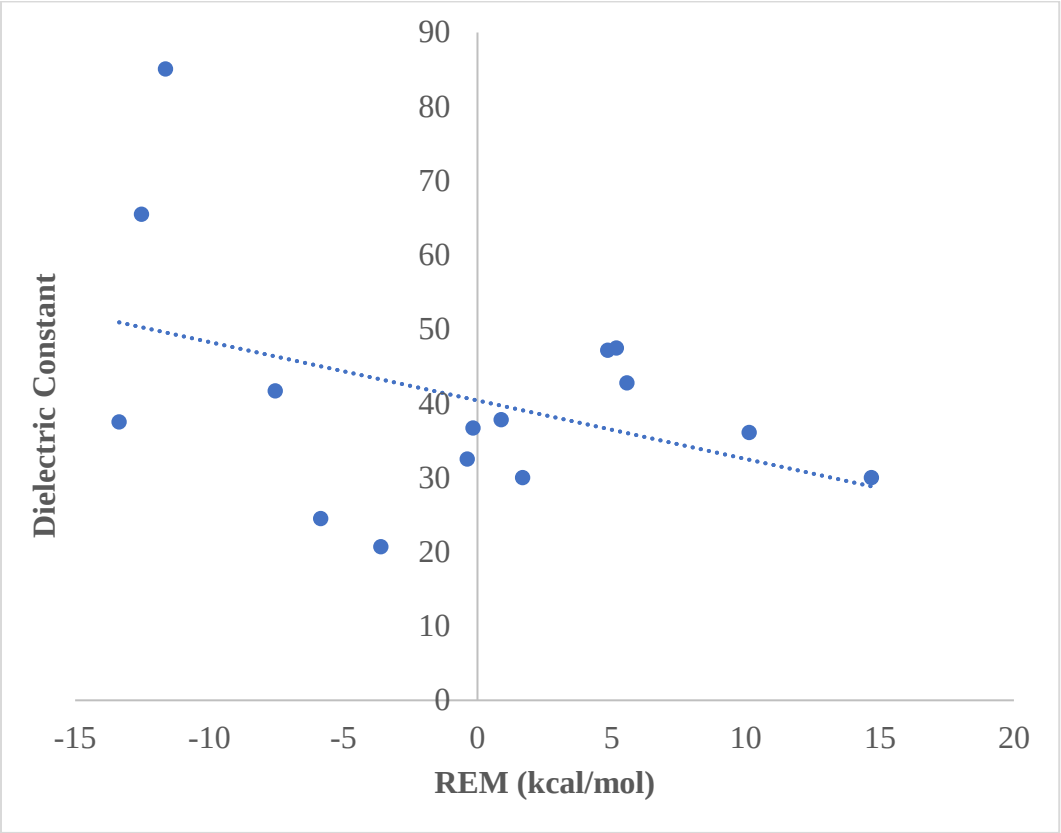

Figure 2.10: Correlation between the dielectric constant and the REM metric for the 16 solvents. Note the poor R^2 value (0.16), denoting a very weak correlation between the variable.

Results from Table 2.13 confirm that the formation of higher–order iodoplumbates is enthalpically preferred in poorly coordinating solvents. In contrast, strong solvents enthalpically prefer to stabilize lower–order iodoplumbate complexes. The solvent 'S–'donor solvents (NMPT and DMTF), which we indicated earlier in this thesis exhibit potentially favourable solvation properties (UMBO and BE), support the formation of lower–order iodoplumbates. In contrast, their oxygen counterparts (NMP and DMF), which we initially identified as moderate solvents, have no clear preference for lower –or higher– order iodoplumbate complexes. As before, one caveat to this metric is that neglecting the choice of A–site cations (MA, FA, or Cs) limits our exploration of the full solution environment, as certain solvents favour the presence of certain cations over others [56].

In general, REM does a good job at predicting the type of complexes formed when the lead halide is dissolved. Its advantage over the UMBO and D_N is the fact the UMBO does not predict the efficacy of all solvents (particularly higher D_N solvents) and the D_N is not available for every solvent. From Figure 2.28, we can also stipulate that a D_N value above 26 is enough to dissolve PbI_2, as indicated by the *y*–intercept of the graph in Figure 2.28. In other words, solvents with a D_N above a value of 26 exhibit a REM value greater than zero, indicating that they have a stronger preference than the halide to bind to the Pb^{2+} center. We determined that, for the UMBO and UMBO of the complex, values of 0.06 and 0.36, respectively, represent suitable cut–off values for good solvents for these two metrics (see Figures 2.29 ad 2.30). No meaningful correlation between the REM and the dielectric constant of these solvents was observed (Figure 2.31), further supporting the idea that the coordination chemistry of the solvent to the Pb^{2+} center is weakly influenced by electrostatics [117]. Overall, using D_N as a metric seems to be good enough for predicting the order of the lead–species observed in solution. But, for an accurate determination

of solvation efficacy, computational metrics like the binding energy (BE) and the relative energy metric (REM) may be more effective in classifying solvents as strong, weak or moderate.

2.5.3 Potential Processing Implications: Effectiveness of Iodide Addition

Benesi−Hildebrand (BH) measurements performed by Hamill Jnr. *et al.* revealed that there is a greater propensity to form higher–order complexes in PC than in DMF [55]. This experimental observation is supported by the average REM results for PC (–3 kcal/mol) and DMF (0 kcal/mol), which indicate that there is a greater enthalpic preference for iodide complexation to the Pb^{2+} in a PC solvent environment than in DMF. The REM results also helps to explain why some solvents are better suited for use as bath solvents or solvent additives [55]. It is very possible that the commonly used tactic of adding excess iodide to a perovskite solution during solution processing would be more effective in some solvent environments over others. Sharenko *et al.* concluded that a greater increase iodide coordination can be achieved by altering the HI: PbI_2 ratio contrary to the MAI: PbI_2 ratio, supplying the system with more iodide, when using DMF as a choice of solvent [126]. However, using this approach in stronger solvent environments (REM > 0) might not yield the same results. Further processing improvements might be required in these environments due to their enthalpic preference to form lower order iodoplumbates. Our results suggest that this is an effective approach for moderate solvents (REM = 0) and poorly coordinating solvent environments (REM < 0), which have an enthalpic preference for iodide coordination over the solvent of choice.

CHAPTER 3

CONCLUSIONS AND FUTURE WORK

3.1 Conclusion

From this study, we confirmed that the strength of the solvent–solute complexes formed in the solution processing of perovskites is more dependent on chemical factors than structurally influenced, *e.g.*, the size of the solvent is not as important as the nature of dative interactions. More specifically, the binding energy of the solvent to the Pb^{2+} center and the Pb–I bond extension (which influences the MBO of the Pb–I bond) reflect the solvent strength; the donor atom binds strongly to the Pb^{2+} center, drawing it further away from the originally bound halide ions. This finding presents a possible explanation for the delayed nucleation observed in poor solvent environments.

This discovery has led us to predict that 'S–'donor solvents are more strongly coordinating than 'O–' donor solvents, confirmed by the Loo group experiments. This fact could be used to improve film morphology by delaying nucleation and growth of the film in solution. For this reason, we recommend the use of NMPT for processing perovskite in solution, the binding energy and UMBO of this solvent warrant its classification as a strong solvent (like DMPU and DMSO). This was confirmed experimentally by the Loo group using EXAFS and SEM techniques, which revealed its preference for coordinating with Pb^{2+} in solution and the favourable morphology of films that were produced using NMPT as a solvent additive.

We have also demonstrated our ability to calculate the Gutmann Donor Number computationally with strong confidence ($R^2 = 0.97$). This has given us the ability to estimate values for the D_N for solvents who have not been experimentally studied for this property. And, from our iodoplumbate studies, we determined that comparing the energies of solvated complexes to PbI_6 iodoplumbate complex reveals the enthalpic preference for solvents over iodides for coordination to the lead salt, which is useful in predicting the type of species one should expect in varying solvent environments. From this, we conclude that strong solvent environments prefer to form lower order iodoplumbates, while poor solvents are enthalpically outcompeted by iodides for Pb^{2+} coordination. Comparing our results to already published Benesi−Hildebrand (BH) measurements conducted by Hamill Jnr, *et al.* supported this conclusion. Lastly, this study also suggested that high D_N solution environments might respond differently to an increase in iodide concentration, and that more process controls might be required to increase iodide complexation in these solutions.

3.2 Future work

We plan to leverage our newly extended force field, SMRFF (Simple Molecular Reactive Force field [132]), to study the distribution of iodoplumbate species in pure solvent environments. This will serve as a test case for the newly developed force field. If successful, it would showcase the advancement of molecular simulation as a route to predict coordination results that the perovskite community had previously used EXAFs and UV–vis experiments to produce. These measurements are both expensive in time and cost and it will serve as a huge advantage to be able

to identify the degree of solvent/halide coordination to the Pb^{2+} center as well as the most abundant plumbate species in solution *via* simulation.

As an extension of our iodoplumbate work, we plan to use SMRFF to generate short–range and long–range parameters relevant to the formation of iodoplumbate complexes in two solvent environments: DMSO (a strong solvent) and GBL (a poor solvent). Experimental results for this system have suggested that iodoplumbates are more likely to form in weakly coordinating solvent environments like GBL and less likely so in DMSO [55, 65, 116]. Computational metrics explored in this thesis, like the binding energy (BE), UMBO and, now, the REM, have also hinted at these preferences. Therefore, we can validate the effectiveness of SMRFF for this reactive system by comparing the most frequent iodoplumbate configuration (higher–order or lower–order) from an MD simulation to experimental observations.

DFT has been successful thus far in revealing the enthalpic preference for iodide complexation in certain solvent environments over others; however, studying their formation in an MD simulation would reveal how temperature and kinetics influence the formation of these complexes in solution. We have outlined two metrics to compare the iodide coordination in DMSO to that in GBL: **Iodide Coordination Ratio** (ICR, ratio of iodides coordinating with Pb^{2+} center to the number of iodides in the system) and **Average Iodide Coordination Number** (ICN, the average number of iodides coordinating with a single Pb^{2+} center).

$$(\text{ICR}) = \frac{\text{Number of Iodides in the system coordinating with } Pb^{2+}}{\text{Total iodides in system}} \qquad \text{Equation 3.1}$$

$$(\text{ICN}) = \frac{\sum_{i}^{N} \text{Iodides coordinating with } Pb^{2+} \text{center (i)}}{\text{Number of } Pb^{2+} \text{atoms}} \qquad \text{Equation 3.2}$$

Example Simulation 1: 90 species (10 PbI_2, 40 **DMSO** molecules, 40 iodide ions)

$$\mathrm{ICR}=\frac{20}{40+20\ (\text{From } PbI_2)}=\frac{1}{3}$$

$$\mathrm{ICN}=\frac{3+2+4+2+4+3+5+2+3+2}{10\ (\text{Number of } Pb^{2+})}=3$$

Example Simulation 2: 90 species (10 PbI_2, 40 **GBL** molecules, 40 iodide ions)

$$\mathrm{ICR}=\frac{40}{40+20\ (\text{From } PbI_2)}=\frac{2}{3}$$

$$\mathrm{ICN}=\frac{5+4+6+4+6+5+6+5+5+2}{10\ (\text{Number of } Pb^{2+})}=4.8$$

From example simulations 1 and 2 in the APPENDIX, the ICR (GBL) > ICR (DMSO) and ICN (GBL) > ICN (DMSO), indicating that the iodide coordination outcompetes solvent coordination in GBL solvent environment, but not in DMSO.

This SMRFF test case will be successful if the ICR (Equation 3.1) and ICN (Equation 3.2) for the GBL solvent environment is higher than the DMSO environment, supported by experimental observations and our REM results. This should also confirm whether the coordination process is more enthalpically driven than by entropic or kinetic factors and showcase the usefulness of SMRFF for reactive systems such as hybrid organic–inorganic perovskites.

BIBLIOGRAPHY

1. Michael Boxwell, *Solar Electricity Handbook: A Simple, Practical Guide to Solar Energy*. Green Stream Publishing, 2012.
2. Schlaich J, Bergermann R, Schiel W, Weinrebe G. Design of Commercial Solar Updraft Tower Systems—Utilization of Solar Induced Convective Flows for Power Generation. ASME. *Journal of Solar Energy Engineering*, 127(1):117–124, 2005.
3. Xinping Zhou, Yangyang Xu. Solar Updraft Tower Power Generation. *Solar Energy*, 128:95–125, 2016.
4. F. Ayub, S. Akhand, A.S. Khan and G. Saklayen. Design and Fabrication of Solar Updraft Tower and Estimation of Power Generation; Initially Focused on Bangladesh. *Earth and Environmental Science*, 150:012023, 2018.
5. Ari Rabl, Carl E. Nielsen. Solar ponds for space heating. *Solar Energy,* 17:1–12, 1975.
6. Lunde, P.J. *Solar thermal engineering: Space heating and hot water systems.* United States: N. p., 1980.
7. Jenny Nelson. *The physics of solar cells*. World Scientific Publishing Co Inc., 2003.
8. Liesbeth Venema. Silicon electronics and beyond. *Nature*, 479:309, 2011.
9. Daryl M Chapin, CS Fuller, and GL Pearson. A new silicon p–n junction photocell for converting solar radiation into electrical power. *Journal of Applied Physics*, 25(5):676–677, 1954.
10. Hugh L Dryden and AE Von Doenho. Solar energy in the exploration of space. *Proceedings of the National Academy of Sciences*, 47(8):1253–1261, 1961.
11. Jeremy N. Munday. The effect of photonic bandgap materials on the Shockley–Queisser limit. *Journal of Applied Physics*, 112:064501, 2012.

12. C.B. Honsberg & S.G. Bowden. *Photovoltaics Education Website*. www.pveducation.org, 2019.
13. Sarah Kurtz and Greg Wilson. Best research–cell efficiencies May 2016.
14. Best Research–Cell Efficiencies. National Renewable Energy Laboratory. NREL solar cell efficiency chart. NREL, 2019.
15. Oxford PV. *Oxford PV – The Perovskite Company*. www.oxfordpv.com, 2019
16. Wei Zhang, Giles E. Eperon, and Henry J. Snaith. Metal halide perovskites for energy applications. *Nature Energy*, 1: 16048, 2018.
17. Samuel D. Stranks & Henry J. Snaith. Metal–halide perovskites for photovoltaic and light–emitting devices. *Nature Nanotechnology*, 10:391–402, 2015.
18. F. Pelayo Garcia de Arquer, Ardalan Armin, Paul Meredith, and Edward H. Sargent. Solution–processed semiconductors for next–generation photodetectors. *Nature Reviews Materials*, 2:16100, 2017.
19. Henry J. Snaith. Present status and future prospects of perovskite photovoltaic. *Nature Materials*, 17:372–376, 2018.
20. Martin A. Green, Anita Ho–Baillie, and Henry J. Snaith. The emergence of perovskite solar cells. *Nature Photonics*, (8):506–514, 2014.
21. Akihiro Kojima, Kenjiro Teshima, Yasuo Shirai, and Tsutomu Miyasaka. Organometal Halide Perovskites as Visible–Light Sensitizers for Photovoltaic Cells. *Journal of the American Chemical Society*, 131(17):6050–6051, 2009.
22. Kim, H.S. *et al.* Lead iodide perovskite sensitized all–solid–state submicron thin film mesoscopic solar cell with efficiency exceeding 9%. *Sci. Rep.*, 2:591, 2012.

23. Yang, W. S. *et al.* Iodide management in formamidinium–lead–halide–based perovskite layers for efficient solar cells. *Science,* 356:1376–1379, 2017.

24. Dianyi Liu and Timothy L. Kelly, Perovskite solar cells with a planar heterojunction structure prepared using room–temperature solution processing techniques. *Nature Photonics*, 8:133–138, 2014.

25. Wei Li, Zheming Wang, Felix Deschler, Song Gao, Richard H. Friend and Anthony K. Cheetham. Chemically diverse and multifunctional hybrid organic–inorganic perovskites. *Nature Reviews Materials,* 2:16099, 2017.

26. Thomas M. Brenner, David A. Egger, Leeor Kronik, Gary Hodes and David Cahen. Hybrid organic—inorganic perovskites: low–cost semiconductors with intriguing charge–transport properties. *Nature Reviews Materials,* 1:15007, 2016.

27. Yuanyuan Zhou, Onkar S. Game, Shuping Pang, and Nitin P. Padture. Microstructures of Organometal Trihalide Perovskites for Solar Cells: Their Evolution from Solutions and Characterization. *The Journal of Physical Chemistry Letters,* 6(23):4827–4839, 2015.

28. Nie, W., Tsai, H., Asadpour, R.; Blancon, J.–C., Neukirch, A. J., Gupta, G., Crochet, J. J., Chhowalla, M.; Tretiak, S., Alam, M. A., Wang, H.–L., Mohite, A. D. High–efficiency solution–processed perovskite solar cells with millimeter–scale grains. *Science,* 347:522–525, 2015.

29. Yan, K., Long, M., Zhang, T., Wei, Z., Chen, H., Yang, S., Xu, J. Hybrid halide perovskite solar cell precursors: Colloidal chemistry and coordination engineering behind device processing for high efficiency. *J. Am. Chem*. Soc., 137:4460–4468, 2015.

30. J. Berry, T. Buonassisi, D. A. Egger, G. Hodes, L. Kronik, Y. L. Loo, I. Lubomirsky, S. R. Marder, Y. Mastai, J. S. Miller, D. B. Mitzi, Y. Paz, A. M. Rappe, I. Riess, B.

Rybtchinski, O. Stafsudd, V. Stevanovic, M. F. Toney, D. Zitoun, A. Kahn, D. Ginley, D. Cahen. Hybrid Organic – Inorganic Perovskites (HOIPs): Opportunities and Challenges. *Advanced Materials*, 27:5102, 2015.

31. Jeon, N. J., Noh, J. H.,Yang, W. S., Kim, Y. C., Ryu, S., Seo, J., Seok, S. I. Compositional engineering of perovskite materials for high performance solar cells. *Nature*, 517:476–480, 2015.
32. Jeon, N. J., Noh, J. H., Kim, Y. C., Yang, W. S., Ryu, S., Seok, S. I. Solvent engineering for high–performance inorganic–organic hybrid perovskite solar cells. *Nature Materials*, 13:897–903, 2014.
33. Dongqin Bi, Soo–Jin Moon, Leif Häggman, Gerrit Boschloo, Lei Yang, Erik M. J. Johansson, Mohammad K. Nazeeruddin, Michael Grätzel and Anders Hagfeldt, Using a two–step deposition technique to prepare perovskite ($CH_3NH_3PbI_3$) for thin film solar cells based on ZrO_2 and TiO_2 mesostructures. *RSC Advances*, 3:18762–18766, 2013.
34. Young Yun Kim, Eun Young Park, Tae–Youl Yang, Jun Hong Noh, Tae Joo Shin, Nam Joong Jeona and Jangwon Seo. Fast two–step deposition of perovskite via mediator extraction treatment for large–area, high–performance perovskite solar cells. *Journal of Material Chemistry A*, 6:12447–12454, 2018.
35. Johannes Schlipf, Pablo Docampo, Christoph J. Schaffer, Volker Körstgens, Lorenz Bießmann, Fabian Hanusch, Nadja Giesbrecht, Sigrid Bernstorff, Thomas Bein, and Peter Müller–Buschbaum. A Closer Look into Two–Step Perovskite Conversion with X–ray Scattering. *The Journal of Physical Chemistry Letters*, 6 (7):1265–1269, 2015.

36. Hsuan–Ta Wu, Yu–Ting Cheng, Ching–Chich Leu, Shih–Hsiung Wu and Chuan–Feng Shih. Improving Two–Step Prepared $CH_3NH_3PbI_3$ Perovskite Solar Cells by Co–Doping Potassium Halide and Water in PbI_2 Layer. *Nanomaterials*, 9(5):666, 2019.
37. C. C. Vidyasagar, Blanca M. Muñoz Flores, Víctor M. Jiménez Pérez. Recent Advances in Synthesis and Properties of Hybrid Halide Perovskites for Photovoltaics. *Nano–Micro Letters*, 10:68, 2018.
38. Schnier, T., Emara, J., Olthof, S., Meerholz, K. Influence of Hybrid Perovskite Fabrication Methods on Film Formation, Electronic Structure, and Solar Cell Performance. *J. Vis. Exp.*, 120:55084, 2017.
39. Apostolos Ioakeimidis, Christos Christodoulou, Martha Lux–Steiner, Konstantinos Fostiropoulos. Effect of PbI_2 deposition rate on two–step PVD/CVD all–vacuum prepared perovskite, *Journal of Solid–State Chemistry*, 244:20–24, 2016.
40. Nguyen T. K. Thanh, N. Maclean, and S. Mahiddine, Mechanisms of Nucleation and Growth of Nanoparticles in Solution, *Chemical Reviews*, 114(15):7610–7630, 2014.
41. Yani Chen, Minhong He, Jiajun Peng, Yong Sun, Ziqi Liang. Structure and Growth Control of Organic–Inorganic Halide Perovskites for Optoelectronics: From Polycrystalline Films to Single Crystals. *Advanced Science*, 3:1500392, 2016.
42. Guangda Niu, Wenzhe Li, Jiangwei Li, Xingyao Liang and Liduo Wang. Enhancement of thermal stability for perovskite solar cells through cesium doping. *RSC Advances*, 7:17473–17479, 2017.
43. Y. Kumar, E. Regalado–Pérez, Arturo Martinez Ayala, N.R. Mathews, Xavier Mathew. Effect of heat treatment on the electrical properties of perovskite solar cells. *Solar Energy Materials and Solar Cells*, 157:10–17, 2016.

44. Young–Hoon Kim, Himchan Cho, Jin Hyuck Heo, Sang Hyuk Im, Tae–Woo Lee. Effects of thermal treatment on organic–inorganic hybrid perovskite films and luminous efficiency of light–emitting diodes. *Current Applied Physics*, 16(9):1069–1074, 2016.
45. Minsu Jung, Sang–Geun Ji, Gwisu Kim and Sang Il Seok. Perovskite precursor solution chemistry: from fundamentals to photovoltaic applications. Chem. Soc. Rev., 48:2011, 2019,
46. Cheng Bi, Yuchuan Shao, Yongbo Yuan, Zhengguo Xiao, Chenggong Wang, Yongli Gao and Jinsong Huang. Understanding the formation and evolution of interdiffusion grown organolead halide perovskite thin films by thermal annealing. *J. Mater. Chem. A*, 2:18508–18514, 2014.
47. Maria Konstantakou, Dorothea Perganti, Polycarpos Falaras and Thomas Stergiopoulos. Anti–Solvent Crystallization Strategies for Highly Efficient Perovskite Solar Cells. *Crystals*, 7(10):291, 2017.
48. Kun–Mu Lee, Chuan–Jung Lin, Bo–Yi Liou, Sheng–Min Yu, Chien–Chung Hsu, Vembu Suryanarayanan. Effect of anti–solvent mixture on the performance of perovskite solar cells and suppression hysteresis behavior. *Organic Electronics*, 65:266–274, 2019.
49. Shao Jin, Yuelin Wei, Feiyue Huang, Xiaomin Yang, Dan Luo, Yu Fang, Yuezhu Zhao, Qiyao Guo, Yunfang Huang, Jihuai Wu. Enhancing the perovskite solar cell performance by the treatment with mixed anti–solvent. *Journal of Power Sources*, 404:64–72, 2018.
50. Dawit Gedamu, Ivy M. Asuo, Daniele Benetti, Matteo Basti, Ibrahima Ka, Sylvain G. Cloutier, Federico Rosei & Riad Nechache. Solvent–Antisolvent Ambient Processed Large Grain Size Perovskite Thin Films for High–Performance Solar Cells. *Scientific Reports* 8:12885, 2018.

51. Taotao Li, Yufeng Pan, Ze Wang, Yingdong Xia, Yonghua Chen, and Wei Huang. Additive engineering for highly efficient organic–inorganic halide perovskite solar cells: recent advances and perspectives. *J. Mater. Chem. A*, 5:12602–12652, 2017.
52. Kang Wang, Zhiwen Jin, Lei Liang, Hui Bian, Dongliang Bai, Haoran Wang, Jingru Zhang, Qian Wang & Shengzhong Liu. All–inorganic cesium lead iodide perovskite solar cells with stabilized efficiency beyond 15%. *Nature Communications*, 9:4544, 2018.
53. Faiazul Haque, Matthew Wright, Md Arafat Mahmud, Haimang Yi, Dian Wang, Leiping Duan, Cheng Xu, Mushfika Baishakhi Upama, and Ashraf Uddin. Effects of Hydroiodic Acid Concentration on the Properties of $CsPbI_3$ Perovskite Solar Cells. *ACS Omega*, 3(9):11937–11944, 2018.
54. A. R. Pascoe, Q. Gu, M. U. Rothmann, W. Li, Y. Zhang, A. D. Scully, X. Lin, L. Spiccia, U. Bach, Y.–B. Cheng, *Sci. China Mater.*, 60:617, 2017.
55. J. Clay Hamill, Jr., Jeffrey Schwartz, and Yueh–Lin Loo. Influence of Solvent Coordination on Hybrid Organic–Inorganic Perovskite Formation. *ACS Energy Letters*, 3(1):92–97, 2018.
56. Tuning Molecular Interactions for Highly Reproducible and Efficient Formamidinium Perovskite Solar Cells via Adduct Approach Jin–Wook Lee, Zhenghong Dai, Changsoo Lee, Hyuck Mo Lee, Tae–Hee Han, Nicholas De Marco, Oliver Lin, Christopher S. Choi, Bruce Dunn, Jaekyung Koh, Dino Di Carlo, Jeong Hoon Ko, Heather D. Maynard, and Yang Yang *Journal of the American Chemical Society*, 140(20):6317–6324, 2018.
57. Jonathon S. Bechtel and Anton Van der Ven. First–principles thermodynamics study of phase stability in inorganic halide perovskite solid solutions. *Phys. Rev. Materials*, 2:045401, 2018.

58. Se–Yun Kim, Hyo Jeong Jo, Shi–Joon Sung, and Dae–Hwan Kim. *APL Materials*, 4:100901, 2016.

59. Priya Srivastava, Anukul P. Parhi, Rahul Ranjan, Soumitra Satapathi, and Monojit Bag. Temperature Assisted Nucleation and Growth to Optimize Perovskite Morphology at Liquid Interface: A Study by Electrochemical Impedance Spectroscopy. *ACS Appl. Energy Mater*, 1(9):4420–4425, 2018.

60. Zhibo Yao, Timothy W. Jones, Mihaela Grigore, Noel W. Duffy, Kenrick F. Anderson, Ricky B. Dunbar, Krishna Feron, Feng Hao, Hong Lin, and Gregory J. Wilson. Tunable Crystallization and Nucleation of Planar $CH_3NH_3PbI_3$ through Solvent–Modified Interdiffusion. *ACS Appl. Mater. Interfaces*, 10(17):14673–14683, 2018.

61. Yu Yu, Songwang Yang, Lei Lei and Yan Liu. Nucleation mediated interfacial precipitation for architectural perovskite films with enhanced photovoltaic performance. *Nanoscale*, 9:2569–2578, 2017.

62. Yongchao Ma, Pesi Mwitumwa Hangoma, Woon Ik Park, Jae–Hong Lim, Yun Kyung Jung, Jung Hyun Jeong, Sung Heum Park and Kwang Ho Kim. Controlled crystal facet of $MAPbI_3$ perovskite for highly efficient and stable solar cell via nucleation modulation. *Nanoscale*, 11:170–177, 2019.

63. Swaminathan Venkatesan, Mehedhi Hasan, Junyoung Kim, Nader R. Rady, Sandeep Sohal, Eric Neier, Yan Yaoc and Alex Zakhidov. Tailoring nucleation and grain growth by changing the precursor phase ratio for efficient organic lead halide perovskite optoelectronic devices. *J. Mater. Chem.* C, 5:10114–10121, 2017.

64. Chongqiu Yang, Yanke Peng, Terrence Simon and Tianhong Cui. Control of PbI_2 nucleation and crystallization: towards efficient perovskite solar cells based on vapor–assisted solution process. *Mater. Res. Express,* 5:045507, 2018.
65. Mayer Bond Order as a Metric of Complexation Effectiveness in Lead Halide Perovskite Solutions James Stevenson, Blaire Sorenson, Varun Hari Subramaniam, James Raiford, Petr P. Khlyabich, Yueh–Lin Loo, and Paulette Clancy. *Chemistry of Materials,* 29(6): 2435–2444, 2016.
66. Henry C. Herbol, Weici Hu, Peter Frazier, Paulette Clancy & Matthias Poloczek. Efficient search of compositional space for hybrid organic–inorganic perovskites via Bayesian optimization. *npj Computational Materials,* 4:51 2018.
67. Paramvir Ahlawat, Pablo Piaggi, Michael Graetzel, Michele Parrinello, and Ursula Rothlisberger. Atomistic Mechanism of the Nucleation of Methylammonium Lead Iodide Perovskite from Solution. *Nature Communications*, 2019.
68. Liu, C.; Wang, K.; Yi, C.; Shi, X.; Smith, A. W.; Gong, X.; Heeger. A. J. Efficient Perovskite Hybrid Photovoltaics via Alcohol–Vapor Annealing Treatment. *Adv. Funct. Mater.*, 26;101–110, 2016.
69. Xiao, Z.; Bi, C.; Shao, Y.; Dong, Q.; Wang, Q.; Yuan, Y.; Wang, C.; Gao, Y.; Huang, J. Efficient, high yield perovskite photovoltaic devices grown by interdiffusion of solution–processed precursor stacking layers. *Energy Environ. Sci.,* 7:2619–2623, 2014.
70. Fu, Y.; Meng, F.; Rowley, M. B.; Thompson, B. J.; Shearer, M. J.; Ma, D.; Hamers, R. J.; Wright, J. C.; Jin, S. Solution Growth of Single Crystal Methylammonium Lead Halide Perovskite Nanostructures for Optoelectronic and Photovoltaic Applications. *J. Am. Chem. Soc.*, 137:5810–5818, 2015.

71. Tosun, B. S.; Hillhouse, H. W. Enhanced Carrier Lifetimes of Pure Iodide Hybrid Perovskite via Vapor–Equilibrated Re–Growth (VERG). *J. Phys. Chem. Lett*., 6:2503–2508, 2015.

72. Zhao, T.; Williams, S. T.; Chueh, C.–C.; Liang, P.–W.; Ginger, D. S.; Jen, A. K.–Y.; deQuilettes, D. W. Design rules for the broad application of fast (< 1 s) methylamine vapor based, hybrid perovskite post deposition treatments. *RSC Adv*, 6:27475–27484, 2016.

73. Li, X.; Dar, M. I.; Yi, C.; Luo, J.; Tschumi, M.; Zakeeruddin, S. M.; Nazeeruddin, M. K.; Han, H.; Gratzel, M. Improved performance and stability of perovskite solar cells by crystal crosslinking with alkylphosphonic acid ømega–ammonium chlorides. *Nat. Chem*, 7:703, 2015.

74. Gardner, K. L.; Tait, J. G.; Merckx, T.; Qiu, W.; Paetzold, U. W.; Kootstra, L.; Jaysankar, M.; Gehlhaar, R.; Cheyns, D.; Heremans, P.; Poortmans, J. Nonhazardous Solvent Systems for Processing Perovskite Photovoltaics. *Adv. Energy Mater*., 6:1600386, 2016.

75. Yi Zhang, Peng Gao, Emad Oveisi, Yonghui Lee, Quentin Jeangros, Giulia Grancini, Sanghyun Paek, Yaqing Feng, and Mohammad Khaja Nazeeruddin. PbI_2–HMPA Complex Pretreatment for Highly Reproducible and Efficient $CH_3NH_3PbI_3$ Perovskite Solar Cells. *Journal of the American Chemical Society*, 138(43):14380–1438, 2016.

76. Lili Zhi, Yanqing Li, Xiaobing Cao, Yahui Li, Xian Cui, Lijie Ci, Jinquan Wei. Perovskite Solar Cells Fabricated by Using an Environmentally Friendly Aprotic Polar Additive of 1,3–Dimethyl–2–imidazolidinone. *Nanoscale Res Lett*, 12:632, 2017.

77. Benjamin J. Foley, Justin Girard, Blaire A. Sorenson, Alexander Z. Chen, J. Scott Niezgoda, Matthew R. Alpert, Angela F. Harper, Detlef–M. Smilgies, Paulette Clancy, Wissam A. Saidie and Joshua J. Choi. Controlling nucleation, growth, and orientation of

metal halide perovskite thin films with rationally selected additives. *J. Mater. Chem. A*, 5:113–123, 2017.

78. Fermi E., Pasta J., Ulam S, Tsingou M. Studies of Non–linear problems. Los Alamos Scientific Lab., N. Mex, 1955.
79. B J Alder and T EWainwright. Studies in Molecular Dynamics. I. General Method. *J. Chem. Phys.*, 31:459, 1959.
80. Orlando Acevedo and William L. Jorgensen. Influence of inter and intramolecular hydrogen bonding on kemp decarboxylations from QM/MM simulations. *Journal of the American Chemical Society*, 127(24):8829–8834, 2005.
81. William L. Jorgensen, David S. Maxwell, and Julian Tirado–Rives. Development and Testing of the OLPS All–Atom Force Field on Conformational Energetics and Properties of Organic Liquids. *J. Am. Chem. Soc*., 118(15):11225–11236, 1996.
82. Density Functional Methods in Physics, edited by R. M. Dreizler and J. da Providencia (Plenum Press, New York, 1985).
83. R. G. Parr and W. Yang. Density–Functional Theory of Atoms and Molecules (Oxford University Press, New York, 1989).
84. P. Hohenberg and W. Kohn. Inhomogeneous Electron Gas. *Phys. Rev.,* 136:864, 1964.
85. W. Kohn and L. J. Sham. Self–Consistent Equations Including Exchange and Correlation Effects. *Phys. Rev.* 140:1133, 1965.
86. Bogdan Mielnika and Marco A. Reyes. The classical Schrodinger equation – *J. Phys. A: Math. Gen*., 29:6009–6025, 1996.
87. E. Schrödinger. An Undulatory Theory of the Mechanics of Atoms and Molecules. *Phys. Rev.*, 28(6):1049–1070, 1926.

88. David, C. W. *Chemistry Education Materials*, 12:1–5, 2006.

89. Neil Qiang Su, Zhenyu Zhu, and Xin Xu. Doubly hybrid density functionals that correctly describe both density and energy for atoms. *PNAS*, 115(10):2287–2292, 2018.

90. Medvedev MG, Bushmarinov IS, Sun J, Perdew JP, Lyssenko KA. Density functional theory is straying from the path toward the exact functional. *Science*, 355:49–52, 2017.

91. Su NQ, Xu X. Development of new density functional approximations. *Annu Rev Phys Chem*, 68:155–182, 2017.

92. Sun J, Ruzsinszky A, Perdew JP. Strongly constrained and appropriately normed semilocal density functional. *Phys Rev Lett* 115:036402, 2015.

93. Burke, K. J. Perspective on density functional theory. *Chem. Phys*., 136:150901–9, 2012.

94. Jeng–Da Chai and Martin Head–Gordon. Long–range corrected hybrid density functionals with damped atom–atom dispersion corrections. *Phys Chem Chem Phys.*, 10:6615–6620, 2008.

95. Zhang Y, Xu X, Goddard WA 3rd, Doubly hybrid density functional for accurate descriptions of nonbond interactions, thermochemistry, and thermochemical kinetics. *Proc Natl Acad Sci USA*, 106:4963–4968, 2009.

96. John P. Perdew. Climbing the ladder of density functional approximations. *MRS Bulletin*, 38(9):743–750, 2013.

97. Douglas M, Kroll NM. Quantum electrodynamical corrections to the fine–structure of helium. *Ann Phys*, 82:89–155, 1974.

98. Kim M–C, Sim E, Burke K. Ions in solution: Density corrected density functional theory (DC–DFT). *J Chem Phys*, 140(18):528, 2014.

99. Neese, F. The ORCA program system. *Wiley Interdisciplinary Reviews.: Comput. Mol. Sci*., 2:73–78, 2012.

100. Jensen, F. In Introduction to computational chemistry; John Wiley & Sons: England, 192:232, 2007.

101. Schaefer, A.; Horn, H.; Ahlrichs, R. J. Fully optimized contracted Gaussian basis sets for atoms Li to Kr. *Chem. Phys*., 1992:97, 2571.

102. Weigand, F.; Häser, M.; Patzelt, H.; Ahlrichs, R. "RI–MP2: Optimized auxiliary basis sets and demonstration of efficiency. *Chem. Phys. Lett*., 294:143–152, 1998.

103. Weigand, F.; Alhlrichs, R. Balanced basis sets of split valence, triple zeta valence and quadruple zeta valence quality for H to Rn: Design and assessment of accuracy. *Phys. Chem. Chem. Phys*., 7:3297–3305, 2005.

104. Grimme, S. Semiempirical GGA–type density functional constructed with a long–range dispersion correction. *J. Comput. Chem*., 27:1787, 2006.

105. Grimme, S.; Antony, J.; Ehrlich, S.; Krieg, H. A consistent and accurate ab initio parametrization of density functional dispersion correction (DFT–D) for the 94 elements H–Pu. *J. Chem. Phys*., 132:154104, 2010.

106. Grimme, S.; Ehrlich, S.; Goerigk, L. Effect of the damping function in dispersion corrected density functional theory. *J. Comput. Chem.*, 32:1456–1465, 2011.

107. Goerigk, L.; Grimme, S. A thorough benchmark of density functional methods for general main group thermochemistry, kinetics, and noncovalent interactions. *Phys. Chem. Chem. Phys*., 13:6670–6688, 2011.

108. Cao, X. B.; Li, C. L.; Zhi, L. L.; Li, Y. H.; Cui, X.; Yao, Y. W.; Ci, L. J.; Wei, J. Q. Fabrication of High–Quality Perovskite Films by Modulating the Pb–O Bonds in Lewis Acid–Base Adducts. *J. Mater. Chem.* A, 5:8416–8422, 2017.

109. Payehghadr, M. & Hashemi, S.E. *J Incl Phenom Macrocycl Chem*, 89:253–271, 2017.

110. Laurence, C. and Gal, J–F. *Lewis Basicity and Affinity Scales, Data and Measurement*. John Wiley & Sons Ltd Publishing, 2010.

111. Davidovich, R. L., Stavila, V., Marinin, D. V.; Voit, E. I., Whitmire, K. H. Stereochemistry of lead (II) complexes with oxygen donor ligands. *Coord. Chem. Rev.*, 253:1316–1352, 2009.

112. Curt M. Breneman and Kenneth B. Wiberg. Determining atom-centered monopoles from molecular electrostatic potentials. The need for high sampling density in formamide conformational analysis. *Journal of Computational Chemistry*, 11(3):361–373, 1990.

113. I. Mayer, Bond order and valence indices: A personal account, *J. Comp.Chem.*, 28:204–221, 2007.

114. Adam J. Bridgeman, Germán Cavigliasso, Luke R. Ireland and Joanne Rothery, The Mayer bond order as a tool in inorganic chemistry, *Chem. Soc., Dalton Trans.*, 0:2095–2108, 2001.

115. S. A. Slivko, M. A. Sarukhanov, and N. N. Kulikova. Structure of the dimethylsulfoxide molecule in neutral, acid, and alkaline media. *J Struct Chem*, 34:363–366, 1993.

116. Sara Rahimnejad, Alexander Kovalenko, Sergio Martí Forés, Clara Aranda, and Antonio Guerrero. Coordination Chemistry Dictates the Structural Defects in Lead Halide Perovskites. *Chem. Phys. Chem.*, 17:2795 – 2798, 2016.

117. Zulqarnain Arain, Cheng Liu, Yi Yang, M. Mateen, Yinke Ren, Yong Ding, Xuepeng Liu, Zulfiqar Ali, Manoj Kumar, Songyuan Dai. Elucidating the dynamics of solvent engineering for perovskite solar cells. *Science China Materials*, 62(2):161–172, 2019.

118. Ingmar Persson, Krzysztof Lyczko, Daniel Lundberg, Lars Eriksson, and Anna Płaczek. Coordination Chemistry Study of Hydrated and Solvated Lead (II) Ions in Solution and Solid State. *Inorganic Chemistry,* 50(3):1058–1072, 2011.

119. Ruven L.Davidovich, Vitalie Stavila, and Kenton H.Whitmire. Stereochemistry of lead(II) complexes containing sulfur and selenium donor atom ligands. *Coordination Chemistry Reviews,* 254(17–18):2193–2226, 2010.

120. Merina K. Corpinot, Rui Guo, Derek A. Tocher, Asma B. M. Buanz, Simon Gaisford, Sarah L. Price, and Dejan–Kresimir Buc. Are Oxygen and Sulfur Atoms Structurally Equivalent in Organic Crystals? *Crystal Growth Des*., 17:827−833, 2017.

121. Vicky Mah and Farideh Jalilehvand. Lead (II) Complex Formation with Glutathione. *Inorg. Chem.*, 51(11):6285–6298, 2012.

122. Petr P. Khlyabich, J. Clay Hamill Jr. Yueh-Lin Loo. Precursor Solution Annealing Forms Cubic–Phase Perovskite and Improves Humidity Resistance of Solar Cells. *Adv. Funct. Mater.,* 28:1801508, 2018.

123. R. Mastria, S. Colella, A. Qualtieri, A. Listorti, G. Gigliab and A. Rizzo. Elucidating the effect of the lead iodide complexation degree behind the morphology and performance of perovskite solar cells. *Nanoscale,* 9:3889–3897, 2017.

124. Liming Wu, Xin–Tao Wu, Ling Chen. Structural overview and structure–property relationships of iodoplumbate and iodobismuthate. *Coordination Chemistry Reviews*, 253(23–24):2787–2804, 2009.

125. Joseph S. Manser, Barry Reid, and Prashant V. Kamat. Evolution of Organic–Inorganic Lead Halide Perovskite from Solid–State Iodoplumbate Complexes. *The Journal of Physical Chemistry C*, 119(30):17065–1707, 2015.

126. Alexander Sharenko, Cameron Mackeen, Leila Jewell, Frank Bridges, and Michael F. Toney. Evolution of Iodoplumbate Complexes in Methylammonium Lead Iodide Perovskite Precursor Solutions. *Chemistry of Materials,* 29(3):1315–1320, 2017.

127. Kevin G. Stamplecoskie, Joseph S. Manser and Prashant V. Kamat. Dual nature of the excited state in organic–inorganic lead halide perovskites. *Energy Environ. Sci.*, 8:208–215, 2015.

128. Iwona Płowaś, Jolanta Świergiel, and Jan Jadżyn. Electrical Conductivity in Dimethyl Sulfoxide + Potassium Iodide Solutions at Different Concentrations and Temperatures. *Journal of Chemical & Engineering Data*, 59(8):2360–236, 2014.

129. Kathryn L. Haas and Katherine J. Franz. Application of Metal Coordination Chemistry to Explore and Manipulate Cell Biology. *Chem Rev*, 109(10):4921–4960, 2009.

130. Leon D. Freedman G. O. Doak G. Gilbert Long Tariq Mahmood Charles B. Lindhal. *Antimony Compounds*. Kirk–Othmer Encyclopedia of Chemical Technology, 2003.

131. Aleksandr V. Marenich, Christopher J. Cramer, and Donald G. Truhlar. Universal Solvation Model Based on Solute Electron Density and on a Continuum Model of the Solvent Defined by the Bulk Dielectric Constant and Atomic Surface Tensions. *The Journal of Physical Chemistry B,* 113(18):6378–6396, 2009.

132. Jovana Andrejevic, James Stevenson, and Paulette Clancy. Simple Molecular Reactive Force Field for Metal–Organic Synthesis. *Journal of Chemical Theory and Computation* 12(2):825–838, 2016.